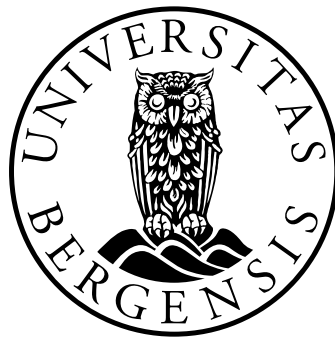# CFD-Model for the Photothermal Conversion Process in Ionic Nanofluids

Melodía Lucas Pérez

The University of Bergen, Department of Physics and Technology
Bergen, Norway

June 2018

A thesis in partial fulfillment of the requirements for the degree of
Master of Science in the subject of Process Technology, Multiphase flows

Acknowledgements

Abstract

Harnessing energy from a sustainable source like the Sun may be one of the key solutions for the increasing demand of energy. However, conventional solar harvesters are relatively low efficient so that use of solar energy is challenging. Several experimental studies have shown in the last decades that the optical and thermophysical properties of the working fluid in solar collectors can be enhanced by adding nano-sized particles. These findings have led to the development of the Direct Absorption Collector (DAC), which is a more promising device compared to the most widely used solar collector, i.e. the flat plate collector. However, a reliable theoretical description of the process phenomena is required for the optimization of the design.

In this research, photothermal energy conversion in nanofluids was numerically studied using a Computational Fluid Dynamics (CFD) model. A DAC of cylindrical shape with incident light on one of its surfaces was adopted for simulations. The Eulerian two-phase transient model included the volumetric absorption of light, losses to the surroundings and the Brownian motion. The validation of the model with experimental data demonstrated low discrepancies.

The model was studied parametrically, altering the extinction coefficient and specific heat of the base fluid, as well as the surface transparency, collector height, solar concentration, particle volume fraction and particle size. The enhancement in efficiency (20%) due to the use of nanofluids was demonstrated by comparison against a selective surface absorption collector. The radiative and convective losses from the DAC surfaces were increased with the nanoparticle volume fraction and with the solar concentration. As the collector height was reduced, the maximum average temperature increased. A maximum temperature of 200.8°C was observed for a 1 cm nanofluid column and 10 sun, where 1 sun equals 1000 W m^{-2}. For a 1 cm solar collector and 2.3 sun, a maximum thermal receiver efficiency of 67% was found for 50 ppm. Increasing the particle size did not lead to a significant enhancement in the receiver efficiency. Nevertheless, it resulted in significant particle deposition. A strong dependency on the

size of the nanofluid column and convection currents was shown. The efficiency was enhanced by 14.5% for the case when the incident light was to the bottom surface in comparison to the case when the incident light irradiated the top surface. The maximum velocity of the dispersed phase was 0.15 cm s^{-1}, which was found for the case when particle concentration was 1.25 ppm.

Finally, design recommendations were presented based on the performed theoretical analysis.

Contents

Chapter 1

Introduction

The worldwide increasing energy demand of energy, together with the fossil fuel emissions concern has led to a growing renewable sources market. The Europe 2030 strategy [1] aim for at least a 27% share of renewable energy consumption and a 40% cut in greenhouse gas emissions compared to 1990 levels. In order to meet these targets, investing in cleaner, low carbon technologies or alternative energy sources is needed. Figure 1.1 shows the energy consumption of renewable sources in Europe from 1900 to 2016. The consumption from renewable sources increased about 3 times. The fact that the Sun is a major source of inexhaustible free energy makes solar energy a promising source to fulfill the increasing demand of energy [2], and its use has increased in Europe in the past 6 years. However, due to the relatively low efficiency of conventional solar harvesters (collectors, ponds and photovotaic cells), use of solar energy is challenging. New cheaper technologies or improving of the efficiency of existing technologies with low additional cost would strengthen the independence from fossil fuels.

The most developed technologies for solar harvesting are photovoltaic cells and thermal collectors. Photovoltaic cells or solar panels absorb the energy form the Sun in a semiconductor material, which produces electricity. Solar thermal collectors are devices that transform the radiation energy from the Sun into internal energy of the working fluid. Unlike the photovoltaic cells, which only can utilize a narrow range of the light spectrum, the solar thermal collectors can generate heat from the Sun across the full spectrum. There are different kind of thermal collectors in use nowadays such as the concentrating type solar collectors, which are used for high temperature applications. This type of collector is characterized by the use of reflecting surfaces, which concentrate the incident radiation at a particular point. A rotary element moves the collector so that the Sun's rays are focused on the absorbing tube along the day. A simpler collector is flat plate type, which does not require moving parts. Its working temperature
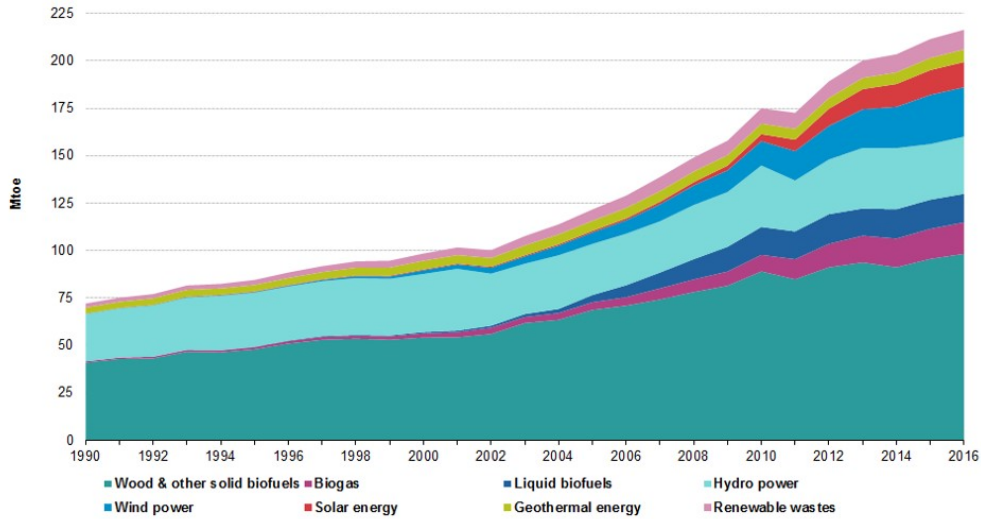
Figure 1.1: Gross inland consumption of renewable sources EU-28 1990-2016 [3].

is lower than concentrating type solar collectors, being suitable for domestic water heating, building heating, crop drying and industrial processing [4]. Despite the declining tendency in solar technology cost, the overall cost still remains high, which makes the use of solar energy challenging. A new kind of solar collectors are direct absorption solar collectors (DAC) (see Figure 1.2). This type of collector is a more promising device compared to the flat plate collectors. The working fluid, which consists of a base fluid and dispersed particles, absorbs directly the incident rays so that the absorber plate is not needed. They present less thermal resistance and a higher efficiency compared to the flat plate solar collectors.

The conventional fluids used in solar harvesters have a low thermal conductivity in comparison to the thermal conductivity of carbon or metals. For instance, carbon nanotubes present a high thermal conductivity, reported to be around 3000 $Wm^{-1}K^{-1}$ [4]. Thus, dispersing particles of these solid materials into the base fluid increases the thermal conductivity of the mixture. As it was introduced by Choi et al. [5], a nanofluid consists on adding nano-size particles to a base fluid. Adding nano-size particles of materials with the desired thermal properties will enhance the heat transfer. Moreover, a receiver with nanoparticles dispersed in the working fluid moves the high temperatures to the interior of the collector, which reduces the surface losses present in conventional receivers. It has been demonstrated by several researchers that the thermal efficiency of solar collectors can be improved significantly by using nanofluids as the working fluid [6, 7, 8].

The idea of suspending particles on a fluid is not new. Since Maxwell's
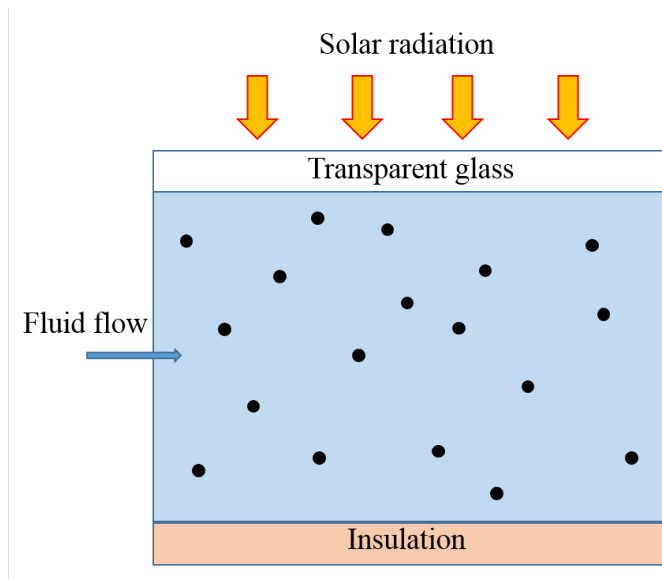
Figure 1.2: Illustration of the working principle of a direct absorption solar collector (DAC).

theoretical work more than a century ago, many theoretical and experimental studies of thermal conductivity in suspensions have been performed. Nevertheless, particles sizes were of millimeter or micrometer order, which introduces, among others, severe abrasion or sedimentation problems in the equipment. A nano-size of these solid particles can assure the stability of the suspension without significant increase of the apparent viscosity and the deposition of particles. In addition to solar collectors [6], it opens a wide range of applications such as distillation [9], thermal storage systems [10] or geothermal energy [11].

Several independent research groups aim their activities at the development of a novel solar generator to produce heat and electricity. Electricity could be produced by use of for instance a turbine, which could utilize the vapour generated in a solar collector. Nevertheless, optimization of the solar generator is hardly possible without a reliable theoretical description of the complex phenomena, which describe the process.

Chapter 2

Basic Theory

According to the definition by Crowe et al. [12], a multicomponent-multiphase flow is a system with a discrete distribution of the macroscopic parameters. Multiphase refers to the mixture of materials with different states of matter, i.e. liquid, solid or gas. Multicomponent refers to the mixture of different chemical species such as carbon, gold or water. In a nanofluid, at least two phases coexist. The fluid flow may consist of more than two phases, for instance solid particles flowing with a liquid and its vapour. In this thesis, the system studied consists of solid particles dispersed in a base liquid fluid. The liquid fluid is referred as the continuous phase, in which properties such as density and velocity vary continuously from point to point. The dispersed phase is defined as the phase, which is not materially connected, i.e. the solid particles.

2.1 CFD

CFD is a complementary approach to pure theory and pure experiment. The CFD approach consists on the use of a numerical technique for solving the governing equations for a given flow geometry and boundary conditions. Each of the equations comes from each of the conservation principles in fluid dynamics and its application to a suitable model of the flow.

The conservation laws can be expressed using an Eulerian approach or a Lagrangian approach. In the Eulerian approach, the flow is determined by analyzing the behaviour of the fluid properties as a function of time. In the Lagrangian approach, the fluid flow properties are determined by tracking a moving control volume as it moves through space and time.

The application of each model will produce a different mathematical statement of the governing equations, which may be more or less convenient for the given application and/or for simulation using CFD. The flow model, where an infinitesimally small element is fixed in space with the fluid

moving through it, leads to the differential form of the governing equations in conservation form. The governing equations in conservation form can all be expressed by the same generic equation, which offers a numerical and computer programming convenience.

The equations and variables (i.e. density, viscosity or pressure) are then discretized. The integral or partial differential equations are replaced with discrete algebraic equations, and the variables are approximated to a fixed number of values. Finally, these equations are solved using numerical algorithms and values for the variables are found at the discrete points.

2.1.1 Governing equations

Determining the appropriate mathematical model describing the physics of the process is one of the key factors. The continuity, momentum and energy equations are mathematical statements of the three fundamental physical principles on which all fluid dynamics is based: conservation of mass, Newton's second law and conservation of energy. This set of equations is known as the Navier-Stokes equations and can be written in conservation form as:

$$\frac{\partial \rho}{\partial t} + \nabla(\rho \mathbf{v}) = 0,$$

$$\frac{\partial(\rho \mathbf{v})}{\partial t} + \nabla(\rho \mathbf{v}\mathbf{v}) = -\nabla p + \nabla(\mu \mathbf{v}) + \rho \mathbf{g} \quad \text{and} \tag{2.1}$$

$$\frac{\partial(\rho e)}{\partial t} + \nabla(\rho e \mathbf{v}) = \nabla(k \nabla T).$$

Here ρ is the density $\mathbf{v}$ is the velocity vector, p is the static pressure field, μ is the dynamic viscosity, e is the specific energy, k is the thermal conductivity coefficient and T is the temperature.

The continuity equation represents the net mass flow out of an infinitesimally small element in x, y and z direction.

The momentum equation comes from applying the conservation of momentum law. The resultant force acting in each direction must equal the mass times acceleration in that direction. Both surface and body forces are included in the derivation of the equations presented above. Body forces refer to all the forces acting on the volumetric mass of the fluid element (such as gravitational or magnetic force), while surface forces act directly on the surface of the fluid element like pressure or viscous forces.

The energy equation is based on the conservation of energy principle. The rate of change of energy inside the element must equal the total energy transfer to or from the surrounding elements.

2.1.2 Boundary and initial conditions

The equations described above govern the flow of a fluid. To be able to solve the particular case object of study, boundary conditions need to be associated with each geometric surface. For instance, for a viscous flow the boundary condition on a surface assumes zero relative velocity between the wall and the fluid immediately in contact with the wall. Then at the surface the expression for the velocity reads:

$$u = v = w = 0, \tag{2.2}$$

where u, v and w are the velocity components in each direction. This boundary condition is known as the no-slip condition [13].

Analogously, the no-slip condition associated with the temperature at the surface reads:

$$T = T_{wall}, \tag{2.3}$$

which means that the temperature of the fluid immediately in contact with the wall. T equals the temperature at the wall T_{wall}. If the temperature of the wall is a function of time, a temperature gradient can be specified as the boundary condition. For instance, for heat conduction using the Fourier law the boundary condition is:

$$\frac{\partial T}{\partial n} = \frac{-q_{wall}}{k_{wall}}, \tag{2.4}$$

where n denotes the direction normal to the wall, q_{wall} the heat transfer to the wall and k_{wall} is the conductivity of the wall. For an adiabatic wall, the heat transfer to the wall $q_{wall} = 0$ is to be inserted in the above equation. Other boundary conditions can be expressed in the same way. In Chapter 5, boundary conditions for conductive and radioactive heat transfer are introduced.

The boundary conditions are applied in each time step. On the other hand, the initial conditions define the starting solution of the whole domain and they are replaced as soon as the solver starts to run. The boundary and initial conditions used in the model are described in Chapter 5.

2.1.3 Discretization and solution

The governing equations are described in this thesis in partial differential form which give the variation of the dependent variables continuously throughout the domain. The mathematical model is transformed into a system of algebraic equations using a discretization technique. The discretization of the governing equations for unsteady problems is done in

space and time. The resulting linear equations can only give answers at a finite amount of points in the domain, grid points, and at a certain time sub-intervals, time-steps.

In Star-CCM+, the finite-volume discretization technique is applied for the solution of multiphase flow [13]. The solution domain is subivided into a finite number of small control volumes, corresponding to the cells of the computational grid. Each grid point is surrounded by a finite volume. The discretized continuum transport equations are applied to each control volume. A set of linear algebraic equations is obtained with total number of unknowns in each equation system corresponding to the number of cells in the grid. The resulting linear equations are then solved with an algebraic multigrid solver. For solving the incompressible Navier-Stokes equations a staggered grid is used. As illustrated in Figure 2.1 the velocity variables v and u are stored at the cell faces, whereas the pressure is located at the cell center. This avoid the decoupling between the pressure and velocity, which is an error of the structured grids leading to checkerboard distribution in the solutions [13].
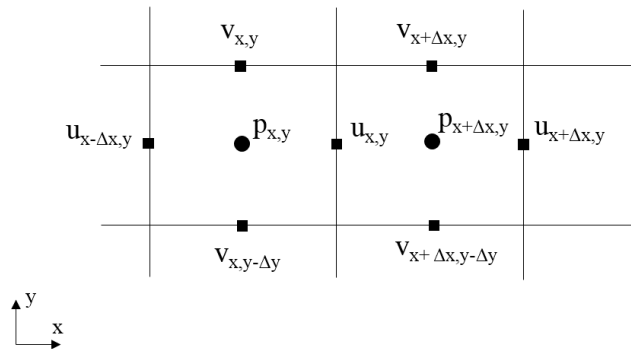
Figure 2.1: Illustration of a staggered grid.

2.1.4 Solver

The discretized equations are solved in this thesis using the Semi-Implicit Method for Pressure Linked Equations (SIMPLE). The SIMPLE algorithm is initiated by setting the boundary conditions and computing an estimation for the velocity and pressure gradients. An intermediate velocity field is then sought by solving the discretized momentum equation. In general, the intermediate velocity field does not satisfy the continuity equation, therefore iterative corrections are necessary. A pressure correction equation is then solved producing cell values for the pressure correction. The

pressure field, velocities and density variations caused by pressure changes are updated using under-relaxation to ensure convergence of the solution algorithm.

2.2 Two-phase flow modelling

Many approaches are found in the literature for modelling solid-liquid mixtures. The simplest method is the single-phase approach, which considers the mixture as a single phase. Empirical properties for the mixture are used for solving the governing equations.

Among the two-phase models, Eulerian-Eulerian and Eulerian-Lagrangian can be distinguished. In the Eulerian-Lagrangian approach each particle in the flow field is tracked and the equation of motion is solved for each individual particle. The mechanisms of the dispersed phase behaviour, such as particle-particle and particle-wall interactions can be included using this method. However it is very computer intensive, so its application is limited to very small systems and/or low amount of particles. On the other hand, in the Eulerian-Eulerian model the dispersed phase is treated as a continuum interpenetrating and interacting with the continuous phase. This method is appropiate to use on a large scale and is less computer intensive. Solid-liquid interactions are straightforward to implement, although modelling of the detailed processes taking place in the dispersed phase is challenging.

In the model used in this research, the Eulerian approach was adopted for both continuous and dispersed phases. Both phases are treated as interpenetrating continua characterized by their volume fraction. The conservation equations are used for each of the phases separately, taking into account the portion of the control volume occupied by each phase.

2.3 Radiative heat transfer in surface and volumetric absorption-based systems

A solar thermal system converts the solar radiant energy into thermal energy of the working fluid. The process can be divided in two steps. First the solar irradiance is absorbed and then the absorbed energy is transferred to the fluid through conductive and convective heat transfer. The radiative heat transfer mechanism is one of the key factors governing the performance of solar harvesters.

Figure 2.2 illustrates schematically the absorption mechanism for surface and volumetric absorption-based systems. In the case of surface ab-
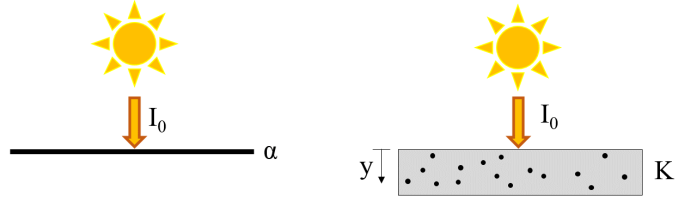
Figure 2.2: Illustration of surface and volumetric absorption mechanisms.

sorption systems, the solar irradiance absorption is characteristic of the surface material. A surface is able to absorb only a part of the incident flux I_0, determined by the absorption efficiency α. The energy absorbed per unit surface is given as:

$$\frac{Q_{absorbed}}{A} = \alpha I_0. \tag{2.5}$$

In the case of volumetric absorption systems, it depends on both the material and the thickness of the layer. The energy absorption can be calculated from the Beer-Lambert law as:

$$\frac{Q_{absorbed}}{V} = BI_0 e^{-Ky}, \tag{2.6}$$

where B is a factor which account for scattered radiation, K is the extinction coefficient and y is the optical path. The extinction coefficient depends, among others, on the particle concentration and size. Thus, the distribution of the particles influences the absorption capability of the nanofluid.

Chapter 3

Literature survey

Numerous studies of nanofluids have been performed in the last decades. Tyagi et al. [14] studied theoretically a direct absorption solar collector using a water-aluminum nanofluid. Their heat transfer analysis revealed the efficiency behaviour with different working parameters. The thickness of the collector was varied from 0.2 to about 5 mm, particle size was considered in the range 1 to 20 nm and volume fraction from 0.1 to 5%. They reported increase of the efficiency with particle volume fraction and collector height. The particle size did not influence significantly the efficiency.

Li et al [15] performed steam generation experiments using $Ag@TiO_2$ dispersed in water. For higher concentrations of solid particles, a higher absorption capacity was reported and a lower evaporation efficiency. This fact was explained by the higher scattered radiation for higher concentrations. A cyclic experiment, refilling the evaporated water after each cycle, conducted by this group shows the well re-usability of the nanofluid considered in their work.

Ni et al. [16] performed experiments and developed numerical and analytical models for low solar concentration (<10 sun, where 1 sun equals 1000 W m^{-2}). They reported a better performance in transient situations for graphitized carbon black and graphene nanofluids (69%) than for carbon black nanofluid.

Liu et al. [17] conducted a combined numerical and experimental study on graphene/ionic liquid nanofluid in a based direct absorption solar collector. The heat transfer model used was close to the experimental results. They attributed temperature discrepancies between numerical and experimental results to convection effects not considered in the model.

The most common approach among theoretical studies within nanofluids has been the single-phase approach, which assumes a thermal equilibrium between the phases and neglects the slip mechanisms between a nano-particle and the host fluid. The results, however, are strongly de-

11

pendent on the effective parameters models obtained from experimental work.

As nanofluids consist of two phases, it is natural to expect some solid-liquid mixture behaviour. With the two-phase approach, interactions between the phases can be included in the model. The fluid and particles are considered as two different phases and different factors can be modelled, such as friction between fluid and particles, Brownian or thermophoretic forces and sedimentation, which affect the thermal behaviour of nanofluids [18]. The continuous phase is usually modelled by an Eulerian model, and the dispersed phase by either an Eulerian or a Lagrangian approach.

Mahdavi et al. [19] performed a numerical study of the hydrodynamic behaviour of nanofluids. They compared the Eulerian mixture model with the Lagrangian model in a steady-state flow. The first one solves only one momentum and one energy equation, while the last one calculates the slip velocity and temperature difference between particles and liquid. For the mixture model, a strong dependency on the empirical nanofluid properties was reported. The Lagrangian approach, which only requires thermophysical properties for the base fluid, showed a better agreement with experiments. A large number of nano-particles present in the nanofluids, even for a low volume concentration, makes the Lagrangian technique hardly applicable for a numerical simulation of the nanofluid-supported DAC, due to enormous computational costs.

Kalthe et al. [20] considered an Eulerian-Eulerian two-phase model to study numerically the nanofluid laminar forced convection in a microchannel. They studied a copper–water nanofluid inside an isothermally-heated parallel plate microchannel. They included virtual mass force and particle-particle interaction force in their model. They observed a negligible relative velocity and temperature between the phases and concluded that the underestimation of the heat transfer enhancement by single-phase approaches is due to the models for the nanofluid properties assumed. The same group [21] also studied aluminia-water nanofluid using a laminar, steady state and two-dimensional Eulerian-Eulerian two-phase model. They concluded that the two phase model were in better agreement with experimental results, in comparison to a single-phase model.

The thermophysical properties of the working fluid determine the performance of nanofluids in different applications. Thermal conductivity, specific heat, viscosity and heat transfer coefficient are the parameters, which has been proved to influence most the nanofluid performance. The behaviour of these properties with temperature, base fluid or particle size, shape and volume concentration is crucial for the selection of appropriate nanofluid in the given operating condition.

Water, ethylene glycol or oil constitute usually the base fluid when

preparing nanofluids. However, the relatively low boiling temperature of water and ethylene glycol limits its use in many applications. The limitation of synthetic oil is due to its high vapour pressure and poor thermal stability. In solar harvesters a working fluid with low vapour pressure and high thermal stability is required.

Ionic liquids are organic salts with low melting points, wide range of liquid temperature, low vapor pressure, and high thermal stability [22]. For instance, 1-hexyl-3-methylmidazolium tetrafluorate ([HMIM]BF$_4$) has a freezing point of around -80°C and a decomposition temperature of 420°C [17]. The shortcoming of ionic liquids, which is poor sunlight absorptivity, can be enhanced by adding nanoparticles which also results on lower viscosity than their base fluids, what is beneficial for their application as heat transfer fluids.

Metals and metals oxides such as Au [23, 24], Ag@TiO$_2$ [15] or Al$_2$O$_3$ [14] have been widely investigated. However, the high thermal conductivity of graphene and its light absorption capability has attracted an increasing attention. In the latest research studies carbon materials have shown the greatest collector efficiency [4]. Wang et al. [22] studied the thermal conductivity enhancement at very low loading of graphene. They prepared highly stable graphene based nanofluids with ionic liquid in ([HMIM]BF$_4$) as base fluid, refer as ionanofluids. They reported an enhancement of over 15% on thermal conductivity which increases as temperature rises.

In this thesis, a transient Eulerian-Eulerian model was adopted to study the photothermal conversion in a DAC under low solar concentration. The DAC consists of a cylindrical container filled with ionic fluid and graphene nanoparticles. The volumetric absorption of incident light and the Brownian motion models were considered. The model was built in the commercial CFD (Computational Fluid Dynamics) software Star-CCM+. A parametric analysis was done by altering the main process determinants.

Chapter 4

Theoretical model

The DAC used in this study consists of a cylindrical container filled with ionic fluid and graphene nanoparticles. A schematic of the volumetric solar receiver is shown in Figure 4.1. The transparent wall receives the incident Sun light which penetrates vertically and is absorbed by the nanofluid. Due to the heat generation from the absorbed radiation of the nanoparticles, the fluid is heated.

The Eulerian-Eulerian two-phase model was adopted to describe the flow and heat transfer of the nanofluid. The volumetric absorption of light, the Brownian motion and the magnetic force were included in the model using the field function tool in Star-CCM+. In this chapter, a detailed description of the mathematical model is shown.

4.1   Governing equations

This section introduces the governing equations of the mathematical model. The Eulerian approach was adopted for both continuous and dispersed phases. The conservation equations were used for each of the phases separately, with the volume fraction, φ, specifying the volume occupied by a phase, where $i = f$ (base fluid) and $i = p$ (nanoparticles).

The continuity equation is written as:

$$\frac{\partial \varphi_i \rho_i}{\partial t} + \nabla(\varphi_i \rho_i \mathbf{v}_i) = 0, \tag{4.1}$$

where ρ is the density, φ is the volume fraction, t is time and $\mathbf{v}$ is the velocity vector. The equations of the phases are related by the following constrain for the volume fraction: $\sum_i \varphi_i = 1$.

The momentum equation reads:
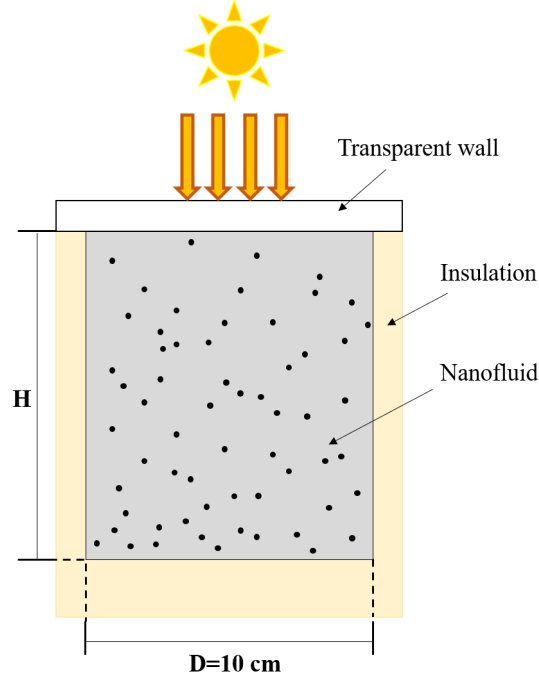
Figure 4.1: Schematic of the volumetric solar receiver. The height of collector, H was varied in the range from 1 to 7.5 cm.

$$\frac{\partial(\varphi_i\rho_i\mathbf{v}_i)}{\partial t} + \nabla(\varphi_i\rho_i\mathbf{v}_i\mathbf{v}_i) = -\varphi_i\nabla p + \nabla(\varphi_i\mu_i\mathbf{v}_i) + \varphi_i\rho_i\mathbf{g} + \mathbf{F}_{D,i} + \mathbf{F}_{B,i}, \quad (4.2)$$

where p is the static pressure field, μ is the dynamic viscosity. $\mathbf{F}_D$ and $\mathbf{F}_B$ are the drag force and the Brownian motion contribution, respectively. They are described later in this chapter.

The energy equation is written as [20]:

$$\frac{\partial(\varphi_i\rho_i e_i)}{\partial t} + \nabla(\varphi_i\rho_i e_i\mathbf{v_i}) = \nabla(\varphi_i k_f\nabla T_i) - q_{interphase,i} + q_{v,i}, \quad (4.3)$$

where e is the specific energy k_f is the thermal conductivity coefficient of the base fluid, T is the temperature, q_v is the volumetric heat generation, and $q_{interphase}$ is the interphase heat transfer rate.

4.2 Interphase momentum and energy transfer

The interphase coupling is described by the interphase momentum and energy transfer. The drag and the Brownian forces describe the interphase momentum transfer.

4.2.1 Drag force

The drag force acting opposite to the relative motion of the particles with respect to the surrounding fluid was modelled as follows:

$$\mathbf{F}_{D,p} = \frac{3}{4} \frac{\mathbf{C_D}}{C_c} \frac{\varphi_p \rho_f}{d_p} |\mathbf{v}_r| \mathbf{v}_r, \tag{4.4}$$

where C_c is the Cunningham correction factor and $\mathbf{v}_r$ is the relative slip velocity between phases. $\mathbf{C_D}$ is the drag coefficient in each direction, which was calculated using the expression given by Schiller-Naumann as [25]:

$$C_D = \begin{cases} \frac{24}{Re_p}(1 + 0.15 Re_p^{0.687}) & Re_p \leq 1000 \\ 0.44 & Re_p > 1000, \end{cases} \tag{4.5}$$

where Re_p stands for particle Reynolds number defined as:

$$Re_p = \frac{\rho_f |v_r| d_p}{\mu_f}. \tag{4.6}$$

The Cunningham correction factor to the drag law can be calculated from:

$$C_c = 1 + \frac{2\lambda}{d_p}(1.257 + 0.4 e^{\frac{1.1 d_p}{2\lambda}}), \tag{4.7}$$

where λ is the molecular free path:

$$\lambda = \frac{\mu_f}{p} \sqrt{\frac{\pi k_B T_f}{2m}}. \tag{4.8}$$

Here m is mass of the base fluid and k_B is the Boltzmann constant.

4.2.2 Brownian motion

For particle sizes smaller than a micron suspended in a fluid, the motion of the particles is affected by the fast moving molecules of the fluid. This results in a random motion due to collisions of molecules with the particles. After a given period of time, the particles subject to Brownian motion will migrate toward the region with smaller concentration [12].

An expression for the Brownian motion following the white Gaussian noise process was developed by Dong et al. [26]. Several investigators have used it in their research studies of nanofluids [27]. The expression for the Brownian motion term in the momentum equation reads:

$$\mathbf{F}_{B,p} = nm_p\xi_i\sqrt{\frac{\pi S_0}{\Delta t}}, \tag{4.9}$$

where n is the number density, m_p is the mass of one particle, ξ_i are zero-mean, unit-variance-independent Gaussian random numbers and Δt is the integration time step. The spectral intensity, S_0, is calculated from:

$$S_0 = \frac{216\mu_f k_B T}{\pi^2 \rho_f^2 d_p^5 \left(\frac{\rho_p}{\rho_f}\right)^2 C_c}. \tag{4.10}$$

Here ρ_p is the density of the particles, ρ_f is the fluid density, d_p is the diameter of the particles, k_B is the Boltzmann constant and C_c is the Cunningham correction factor.

4.2.3 Interphase heat transfer

The heat transfer between the solid dispersed phase and the fluid continuous phase can be calculated as [25]:

$$q_{interphase,i} = \frac{6\varphi_p h_{int}(T_i - T_j)}{d_p}, \tag{4.11}$$

where h_{int} is the mean surface average heat transfer coefficient, which can be calculated as a function of the continuous phase thermal conductivity k_f, the Nusselt number Nu_p, and the diameter of particles d_p [25]:

$$h_{int} = \frac{k_f Nu_p}{d_p}, \tag{4.12}$$

where d_p is the diameter of the particles and k_c is the continuous phase thermal conductivity. Nu_p is calculated using the Ranz-Marshall correlation:

$$Nu_p = 2 + 0.6Re_p^{0.5}Pr^{0.3}. \tag{4.13}$$

Pr is the Prandtl number defined for as:

$$Pr = \frac{C_p\mu_f}{k_f}, \tag{4.14}$$

where C_p is the thermal conductivity of the continuous phase.

4.3   Volumetric heat generation

Scattering term becomes negligible for the extremely small particle size used in nanofluid applications. Therefore, the attenuation of electromagnetic energy is predominantly due to absorption by the nanoparticles and is mathematically given by the Beer-Lambert law.

The volumetric heat generation, q_v, corresponds in this case to the energy absorbed by the nanofluid. It is calculated using the Beer-Lambert law for light absorption, which introduces an exponential heat generation term in the energy equation [16]:

$$q_{v,i} = \varphi_i I_0 K_i e^{-\left(K_f + K_p\right)y}, \tag{4.15}$$

where y refers to the optical path and its coordinate reference frame is at the surface which receives the light. I_0 is the incoming radiation and K_f is the extinction coefficient of the base fluid. The extinction coefficient of the particles, K_p, was calculated as [28]:

$$K_p = 6\frac{\varphi_p}{d_p}. \tag{4.16}$$

Chapter 5

Numerical procedure

An effective CFD simulation, which delivers meaningful and reliable results depends on multiple factors, such as boundary conditions specifications, mesh quality and time step. This chapter describes the problem description which, together with the governing equations specified in the previous chapter, will reproduce the simulation model required for the study.

5.1 Geometry

The direct solar absorption collector chosen as the model for the present simulations corresponds to the one in the paper published by Liu et al. [17]. Due to the experimental data available for validation from the paper, the same geometry was adopted. It is illustrated in Figure 4.1. The receiver consists of a cylindrical container isolated in all its surfaces except the top one, which is an open surface. The cylinder has a diameter of 10 cm, while the height can be varied. For comparison of the temperature profiles with the experimental results, two height of collector: 7.5 cm and 3.8 cm were simulated. An extra model with a height of 1 cm was also considered in order to investigate the effect of the geometry on the absorption process.

5.2 Boundary conditions

In order to reduce the computational domain and thus, computational time, symmetry boundary conditions were used in the model. Two symmetry planes make possible to reduce the model of the real experimental geometry.

With respect to the flow, each of the remaining walls are associated with the boundary condition known as the no-slip condition. This boundary condition for viscous flow assumes zero relative velocity between the surface
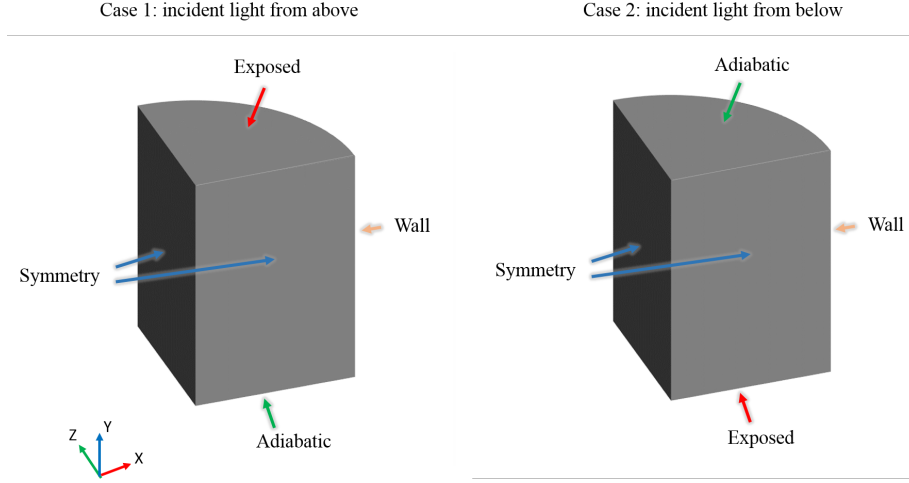
Figure 5.1: Illustration of the boundaries for incident light from above (Case 1) and from below (Case 2).

and the phase immediately at the surface. As none of the surfaces move, this implies that at the wall, for each phase:

$$u = v = w = 0. \tag{5.1}$$

In addition, boundary conditions for temperature of the layer immediately in contact with the wall of the container are needed. Different boundaries are defined for each of the surfaces.

The wall parallel to the heating surface is assumed to be adiabatic. This means that there is no heat transfer to the surface. Hence, the temperature gradient at that wall becomes zero:

$$\left.\frac{\partial T}{\partial y}\right|_{adiabatic} = 0. \tag{5.2}$$

The side of the container was in the experiments [17] insulated using a low-density foam. Thus the temperature of the wall is not known, but the instantaneous heat flux is considered to be constant through an axis perpendicular to the wall. The temperature at the inner wall is then associated with the boundary condition:

$$\left.k\frac{\partial T}{\partial n}\right|_{wall} = h_v(T_f - T_{wall}), \tag{5.3}$$

where n is the direction normal to the wall, k is the conductivity of the insulation material, h_v is the heat transfer coefficient corresponding to the air around the receiver and T_{wall} stands for the temperature at the outer surface.

The heat transfer coefficient can be calculated as:

$$h = \frac{Nu k_{wall}}{H};$$

(5.4)

where H is the height of the receiver and Nu is the Nusselt number, which for a vertical cylinder:

$$Nu = a(GrPr)^b,$$

(5.5)

where a and b are constants dependent on Gr, Grashof number, and Pr, Prandtl number.

$GrPr$	a	b
$10^4 - 10^9$	0.59	0.25
$10^9 - 10^{12}$	0.13	0.33

Grashof number is defined as:

$$Gr = \frac{H^3 \rho_f g \beta_f \Delta T}{\mu_f^2},$$

(5.6)

where β is the coefficient of thermal expansion, which can be calculated using the ideal gas assumption as the inverse of the temperature. ΔT is the absolute value of the difference in temperature between the outer surface of the cylinder and the ambient temperature.

Assuming the analogous no-slip condition associated with the temperature at the surface, the temperature of the layer immediately in contact with the surface will equal the temperature at that surface.

At the top surface of the receiver, in addition to conduction and convection, thermal re-radiation was considered, as there was no insulation in that surface [17]:

$$k \frac{\partial T}{\partial y}\bigg|_{exposed} = h_{exposed}(T_{exposed} - T_{amb}) + \varepsilon \sigma (T_{exposed}^4 - T_{amb}^4),$$

(5.7)

where k is the thermal conductivity, h_{top} is the natural convective heat loss coefficient associated to the air over the receiver, ε is the emissivity of the receiver, σ is the Stefan-Boltzmann constant, $T_{exposed}$ and T_{amb} are, respectively, the temperatures at the exposed surface of the receiver and ambient.

For the horizontal plate receiver [17], $h_{exposed}$ can be calculated depending on the Rayleigh number as follows:

$$h_{exposed} = \begin{cases} \frac{k_f}{D} 0.54 Ra^{\frac{1}{4}} & Ra \leq 10^7 \\ \frac{k_f}{D} 0.15 Ra^{\frac{1}{3}} & Ra > 10^7 \end{cases},$$

(5.8)

where D is the diameter of the horizontal plate receiver and Ra is calculated as:

$$Ra = \frac{g|(\frac{\partial \rho_a}{\partial T})_p|\rho_a C_{pa}|T - T_{amb}|D^3}{k_a \mu_a}, \tag{5.9}$$

where ρ_a, $C_{p,a}$, k_a and μ_a are the density, specific heat, thermal conductivity and viscosity of the air around the receiver.

5.3 Thermophysical properties and initial conditions

For the base fluid the variation of the properties with temperature was considered using the expressions shown in the following.

Thermal conductivity was calcuated using the model:

$$k_f = 0.104 + 2.140 \cdot 10^{-4}T.$$

Specific heat was found using:

$$c_{p,f} = 1843.1 + 1.4959T.$$

Density of the fluid was calculated from:

$$\rho_f = 1301.2 - 0.586T.$$

Viscosity was computed from:

$$\mu_f = \begin{cases} 0.19 & T < 298 \\ 24.687e^{-0.04T} & 298 \leq T \leq 420 \\ 0.02 & T > 420 \end{cases}$$

with T in K.

For comparison with the experimental work by Liu et al. [17] the thermophysical properties of graphene listed in Table 5.1 were used in this thesis. The properties were assumed to be temperature independent. The particles were assumed as spheres and of uniform size. The volume fraction was 2.5 ppm (1 ppm $= 10e^{-6}$). Sensitivity analysis of the properties was performed to investigate the influence on the collector performance.

The initial conditions included: uniform temperature field 290.2 K, zero velocity and atmospheric pressure.
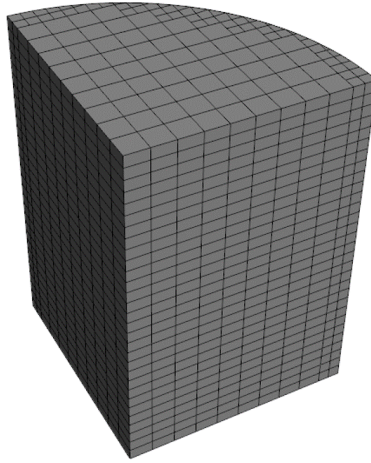
Table 5.1: Properties of graphene nanoparticles

Diameter [nm]	500
Density [kg m^{-3}]	2250.0
Heat capacity [J kg^{-1} K^{-1}]	707.68
Thermal conductivity [W m^{-1} K^{-1}]	24

5.4   Mesh

Figure 5.2 illustrates the mesh generated. Hexahedral cells were used for discretization of the domain. A finer grid was use close to the wall enclosing the cylinder.

Figure 5.2: Illustration of the mesh with a base size of 5 mm.

A grid independence study was done by varying the base size between nodes. The results are shown in table 5.2, where the average temperature of the bulk fluid was used as control variable. A base size of 0.005 was considered in this research, because reducing the base size to 0.004 would not lead to more precise results while the computational time would be much longer.

Table 5.2: Grid-independence study. Results for 7.5 cm height receiver.

Base size	Cells	Average temperature °C
0.004	7942	19.313
0.005	3840	19.314
0.006	2652	19.321

5.5   Numerical method

The numerical model was built in the commercial software Star-CCM+. The discretization of the governing equations in space was done by a finite volume technique with 3840 hexahedral cells and an implicit advancement in time with a step of 5 ms. The equations were solved using the SIMPLE numerical technique. For accelerating the convergence, an under-relaxation of 0.7 was used for the phase coupled velocity and of 0.3 for pressure.

Chapter 6

Validation and results

The model was validated against experimental results and studied parametrically. In this Chapter, the validation of the model and the influence of different parameters on the collector performance are shown.

6.1 Validation of the model

Liu et al. [17] developed an experimental set up consisting of a cylindrical receiver with a solar simulator placed on top. The solar simulator provided different solar concentrations in the range 1 to 10 sun. Thermocouples were located along the height of the receiver and spaced 1 cm apart. The geometry that they used for experiments was adopted for the present numerical study and is described in the previous section. In the theoretical model, light incided on the top surface as in the experiments. The temperature was calculated on a vertical line centered in the cylindrical collector. The temperature profiles were calculated at the same time increments as for the experimental results. Two models were used for validation: the first one with height of collector 7.5 cm and graphite concentration 2.5 ppm, and the second one for 3.8 cm and 5 ppm. In both cases the considered solar concentration was 2.3 sun. The validation of the computer code is shown in Figure 6.1 where the experimental results [17] are compared with the CFD simulations. The continuous lines represents the numerical results from the model (Mod) and the dots represent the experimental work (Exp) [17].

The highest temperature was found on top of the receiver. At the bottom of the collector, the temperature remained constant even after 1000 s of exposure, leading to a more pronounced temperature gradient with time. This behaviour was expectable since the light beam attenuates exponentially as it travels trough the nanofluid column according to the Beer-Lambert law.

The model predicts the temperature in the receiver with less than 8% discrepancy. The extinction coefficient was assumed constant over the entire wavelength spectrum, which is the main reason of discrepancies.
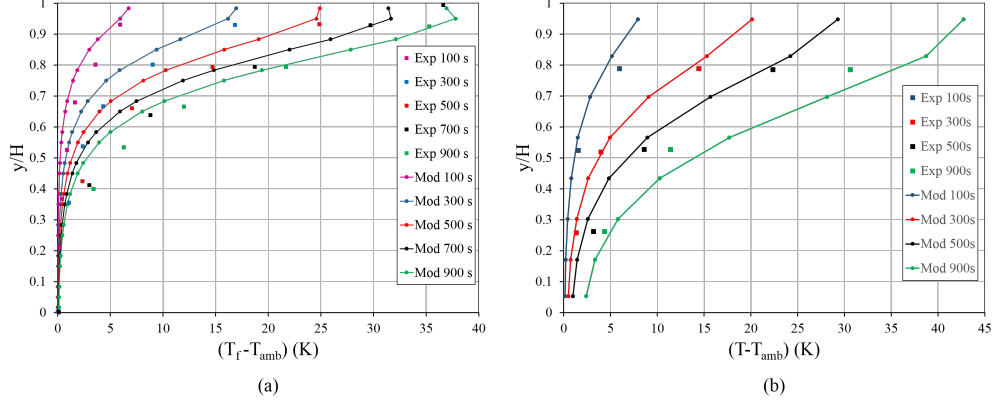
Figure 6.1: Nanofluid temperature profile in the axial direction. Simulation results (Mod) are compared with experiments (Exp) at 100, 300, 500, 700 and 900 s of the heating process for: H=7.5 cm, φ_p=2.5 ppm (a); and H=3.8 cm, φ_p=5 ppm (b).

6.2 Results

Average temperatures were calculated using volume averaged values. The thermal efficiency of the solar receiver, defined as the ratio between the collected thermal energy to the total incident energy [17], was used for comparison of the cases studied. It reads:

$$\eta = \frac{mC_p\left(T_{bulk} - T_{amb}\right)}{\int_0^t I_0 A dt},$$
(6.1)

where, m and C_p are the mass and heat capacity of the base fluid.

6.2.1 Influence of the extinction coefficient

A comparison between various values of extinction coefficient for the base fluid is shown in Figure 6.2. As the extinction coefficient increases so does the maximum heat absorbed at the top of the receiver, while the heat absorbed below the first 20% of nanofluid column decreases. This is due to the exponential form of the volumetric heat absorption expression. For a collector height lower than about 1.5 cm, a larger extinction coefficient clearly leads to a larger average volumetric heat absorbed. It was enhanced by 41.5 kW m^{-3} when increasing the extinction coefficient from 20 to 80

m^{-1}. For a higher nanofluid column the average volumetric heat absorbed was only enhanced by 2.5 kW m^{-3}. The same trend was observed for the temperature profiles. The temperature gradient was more pronounced for a higher extinction coefficient. The maximum temperature at the top of the receiver was found for the highest extinction coefficient, while at the bottom of the receiver it was found for the lowest value. As a result, the average temperature after 1000 s of the heating process was slightly reduced from 27.92 to 27.59°C when increasing the extinction coefficient of the continuous phase from 20 to 80 m^{-1}. Accordingly, the efficiency was enhanced by 2.7% when reducing the extinction coefficient.
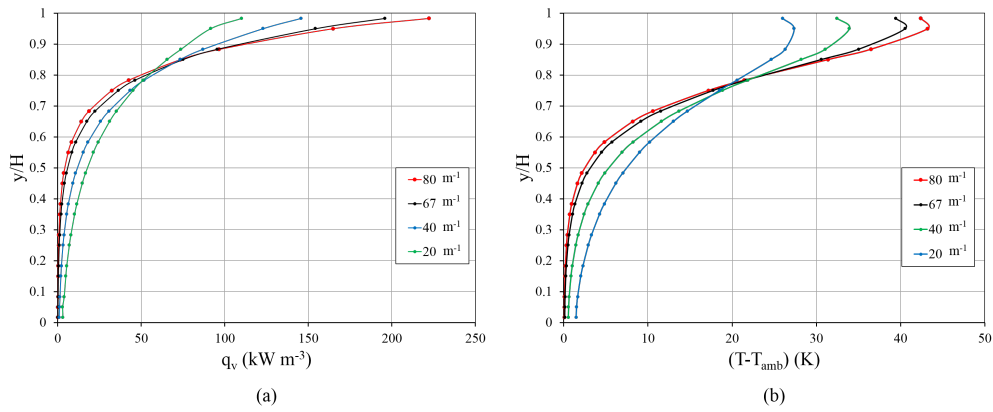

Figure 6.2: Heat absorbed by the nanofluid (a) and temperature profiles in the axial direction (b) for different vales of extinction coefficient of the base fluid.

6.2.2 Influence of the specific heat

The specific heat of the base fluid was modelled as a function of temperature using a polynomial expression, which was described previously. In addition, the effect of the specific heat on the heating process was examined in the range from 1242 to 4000 J kg^{-1} K^{-1}, assuming it was a constant.

Figure 6.3 shows the temperature profiles and the thermal receiver efficiency comparisons for various values of the specific heat. "Polynomial in T" case when the polynomial expression was used. As the specific heat increases, the temperature gradient and the temperature at the top surface of the receiver decrease. Increasing the specific heat from 1243 to 4000 J kg^{-1} K^{-1} led to a reduction of 30.29 K at the top surface of the receiver. This was expectable since a substance with lower specific heat requires less energy to raise or lower its temperature. The slight decrease in temperature at the top surface can be explained by the fact that a mixed conductive and radiative boundary condition was used at the exposed surface.
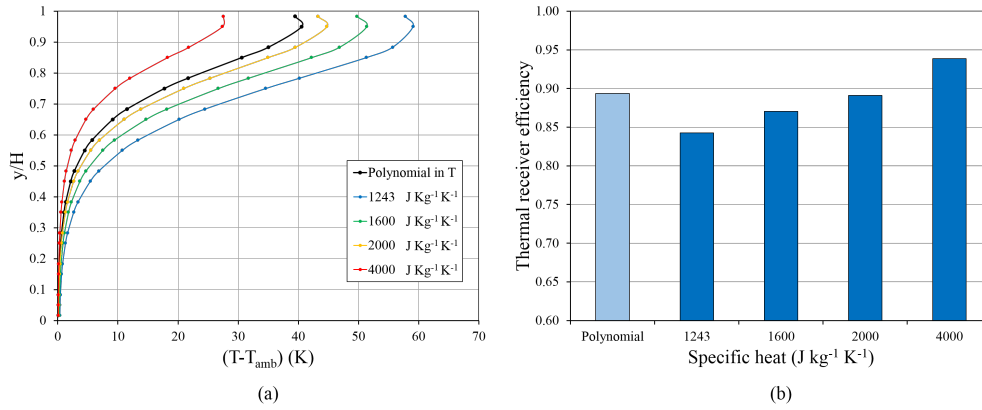
Figure 6.3: Temperature profiles in the axial direction (a) and thermal receiver efficiency (b) for different vales of specific heat of the base fluid after 1000 s of the heating process.
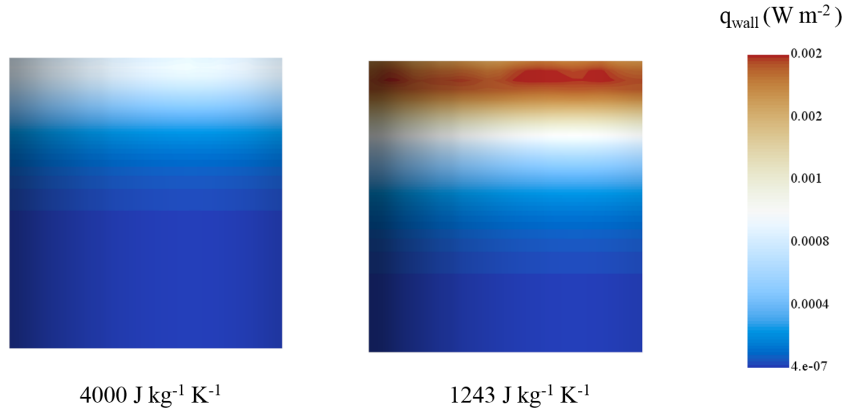
Figure 6.4: Heat loss per unit area at the wall surface for a specific heat of the base fluid of 1243 and 4000 J kg^{-1} K^{-1} after 1000 s of the heating process.

The heat loss per unit area at the wall surface is illustrated in Figure 6.4 for 4000 and 1243 J kg^{-1} K^{-1}. For a specific heat value of 1243 J kg^{-1} K^{-1} the losses to the surroundings at the side wall did not exceed 0.02 W m^{-2}, while at the top wall the heat flux was about 1.3 W m^{-2}. Due to the insulation at the sides of the receiver, the highest losses were found from the exposed surface because of radiation and convection. The heat losses gradient tendency was congruent with the temperature gradient in the axial direction of the receiver, being negligible at the bottom of the receiver. The lower temperatures for an specific heat value of 4000 J kg^{-1} K^{-1} resulted in a maximum heat flux to the surroundings of 0.53 W m^{-2}. In consequence, as the same heat was absorbed for the different specific heat values, the thermal receiver efficiency increased as the specific heat was

increased. The thermal efficiency was enhanced by 10% when the specific heat was increased from 1243 to 4000 J kg^{-1} K^{-1}.

6.2.3 Influence of natural convection

In a gravitational field, natural convection occurs due to temperature differences, which affect the density, and thus the relative buoyancy of the fluid. Components with higher density descend, while components with lower density rise, leading to bulk fluid movement [25].

In this thesis, the influence of natural convection in the collector was studied by comparison with a case where the bottom surface was exposed to the Sun radiation. A mixed convective and radiative boundary condition was used to model the bottom surface. The top surface was assumed adiabatic.
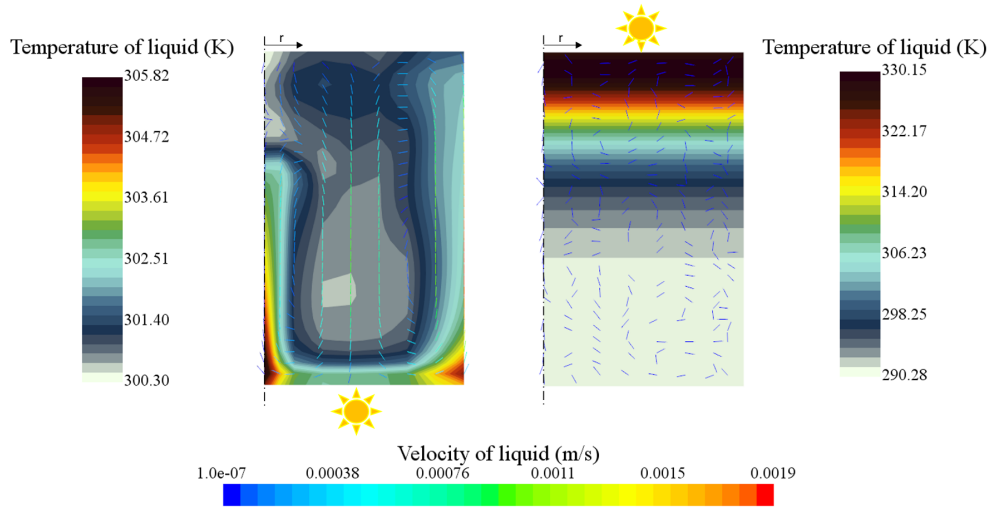
Figure 6.6 shows the temperature distribution and nanoparticle velocity vectors in the midline cross-section of the DAC. For the case with incident light at the top surface, the velocity magnitude was negligible but the temperature variation along the y-axis was significant. In Figure 6.5, the temperature profile after 1000 s was compared with a case where there was no movement in the flow. There was almost no difference in the temperature profiles. Thus, the velocity of the fluid when incident light is at the top surface is negligible and the heat transfer mechanism is only due to conduction.
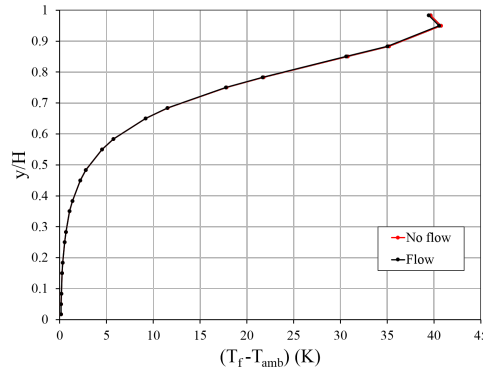
Figure 6.5: Nanofluid temperature profile in the axial direction after 1000 s of light exposure with and without fluid flow in the receiver.
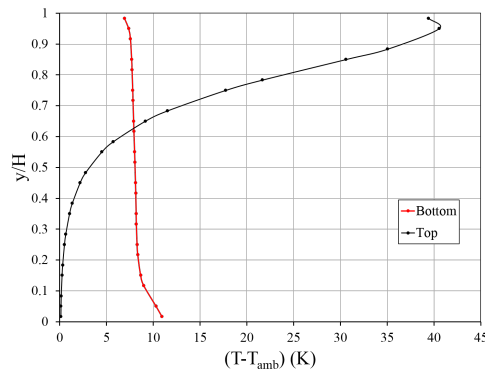
With the incident light to the bottom surface, convective currents were found during the simulation, which led to a more uniform temperature profile. The average bulk temperature was 0.3 K higher for this case.

The temperature profiles of the nanofluid in a midline in the axial direction are shown in Figure 6.7. The temperature difference between the

Figure 6.6: Temperature distribution and velocity vectors when incident light is at the bottom (left) and at the top of the receiver (right) after 1000 s of the heating process.

top and bottom surfaces reduced from 39.3 to 3.4 K, so that the losses to the surroundings were limited.

Figure 6.7: Nanofluid temperature profile in the axial direction after 1000 s of exposure to incident light to the bottom and to the top of the receiver.

Figure 6.8a illustrates the bulk average temperature increment with respect to the ambient temperature. The average temperature was 0.86 K higher after 1000 s of exposure when the bottom surface was exposed to 2.3 sun. The efficiency of the thermal collector evolution with time is shown in Figure 6.8b. The decrease in thermal receiver efficiency is more pronounced when incident light is at the top surface after about 200 s. This can be explained from the fact that after 200 s natural convection was fully developed. The efficiency was enhanced by 14.5% with respect to the case

32
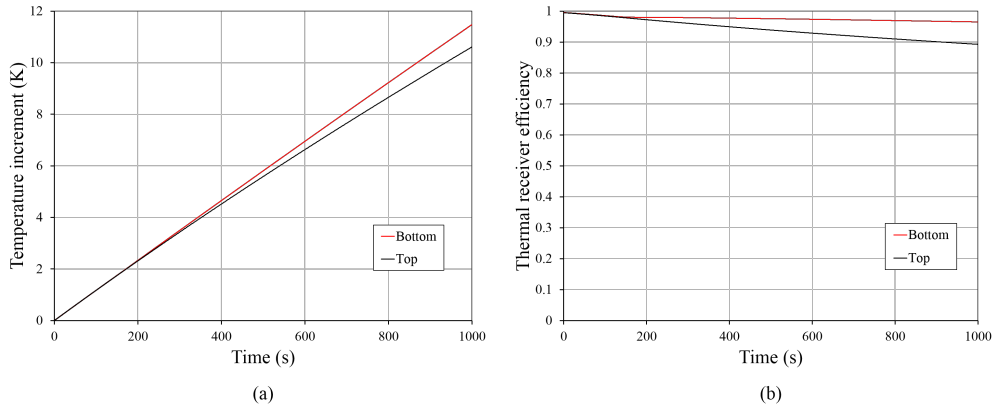
Figure 6.8: Average bulk temperature increment with respect to the ambient temperature (a) and thermal receiver efficiency (b) as a function of time with incident light to the bottom and to the top of the receiver.

when the incident light was at the top surface after 1000 s of exposure. The difference is caused by the more uniform temperature profile when heating from the bottom. When heating from the top, the warmer area is on top of the receiver, which as mentioned above, is not isolated. This leads to higher losses.

The stirring of the fluid due to natural convection results in a better efficiency, as it has been discussed previously. Another way to achieve the particles motion could be the use of magnetic nanofluids along with a magnetic field to attract the particles towards the hot area. Some researchers have focused their studies on this effect, introducing a concept known as thermomagnetic convection. This term is associated to the flow in the fluid induced by the magnetization of magnetic nanofluids. The magnetization of the magnetic nanoparticles is a function of temperature. Thus, the temperature gradient induces spatial magnetization gradients [29]. This effect offers the possibility of controlling the fluid flow by applying an external magnetic field.

6.2.4 Influence of the volumetric absorption

To elucidate the benefits of volumetric absorption in DACs when using nanofluids, the results were compared to a surface absorption collector. A volumetric absorption system consists of a transparent cover and a nanofluid bath below, and the characteristics used for simulation have been described before. On the other hand, a surface absorption system consists of a base fluid bath and a solar selective surface. The solar radiation is converted into heat at the solar selective surface and later transferred to the working fluid.

33

Capturing the sunlight as heat using selective absorbers involves absorbing most of the solar wavelengths under standard atmospheric conditions, while suppressing infrared re-radiation induced by heating of the selective absorber. The efficiency of this process relies on the selection of the appropriate combination of materials. For illustration an absorption of 0.8 and an emissivity of 0.12 was adopted in this thesis [30]. The emissivity determines the losses to the surroundings due to radiation. A heat flux αI_0, where α is the absorption efficiency and I_0 is the incident light, was considered at the exposed boundary condition. A negligible particle concentration was assumed and the volumetric absorption term was set to zero.
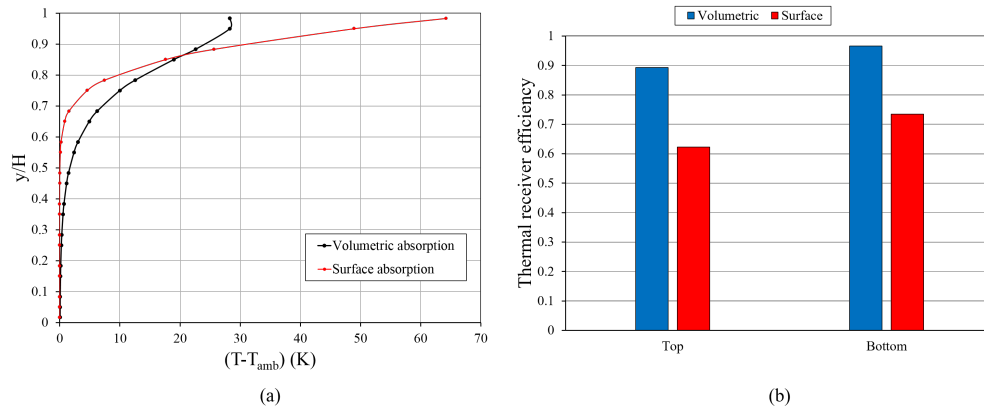
Figure 6.9: Temperature profile comparison when considering volumetric or surface absorption of the incident light (a). Efficiency comparison for surface and volumetric absorption when radiating from the top or from the bottom surface (b).

Figure 6.9.a shows the volumetric absorption temperature profile comparison with the surface absorption for the incident light at the top. The average temperature for surface absorption was over 3.2°C lower, while the maximum temperature was larger, decreasing significantly within the first 2 cm of nanofluid column. As a result, the total heat loss to the surroundings was about 1.14 W, while for the nanofluid volumetric absorption the loss decreases to 0.8 W.

For both cases considered: incident light on top or bottom surface, the thermal receiver efficiency was enhanced over 20% for the volumetric absorption receiver as shown in Figure 6.9b. Even though the emissivity of solar selective surfaces is much lower than for nanofluids [31], the localization of high temperatures into the interior of the receiver resulted in lower radiative losses for the case of volumetric absorption.

6.2.5 Influence of the collector height

An important model specification is its size. The height of the solar collector influences the heat absorbed by the nanofluid and its thermo-hydraulic behaviour. Simulations were performed for different heights of collector, particularly for: 7.5, 5.0, 3.8 and 1.0 cm. The incident light on the top surface was 2300 W m^{-2}, particle size was 500 nm and the volume fraction 2.5 ppm.

The volumetric heat absorbed by the nanofluid in W m^{-3} throughout the nanofluid column is illustrated in Figure 6.10. Most of the heat is absorbed within the first 10% of nanofluid column. The lower section does not absorb any of the incoming light.
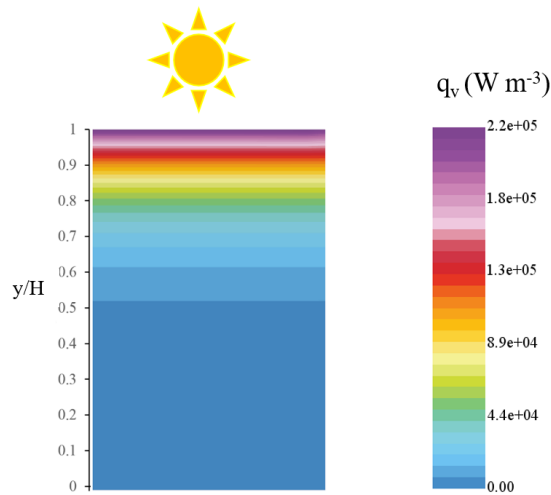
Figure 6.10: Volumetric heat absorbed by the nanofluid in W m^{-3}. H=7.5 cm.

Figure 6.11a shows the temperature profiles for receivers of different heights. As the collector height increases, the temperature gradient along the vertical axis also increases. This behaviour was expected as, for a nanofluid column larger than approximately 3.8 cm, the light beam attenuates before reaching the bottom (Figure 6.10). For 1 cm collector the temperature was nearly uniform in the fluid inside the collector. This is due to relatively short distance the light beam has to go through, without relatively large attenuation. For 3.8 cm and 5 cm, a slightly increment in temperature at the bottom was found. As there was no light absorbed at the bottom of the receiver for 5 cm, the enhancement in temperature at the lower section was caused by the higher temperature of the nanofluid layers above. For the 7.5 cm receiver, the temperature at the bottom remained

constant even after 1000 s of exposure.

The heat loss as a function of height is shown in Figure 6.11b together with the heat absorbed for the different collector heights considered. For a larger collector height, the total heat absorbed by the nanofluid was larger. However, the increment is not pronounced after 3.8 cm because of the attenuation of the light beam, as it was mentioned previously. The temperature of the bulk fluid increased from 27.6 to 62.6°C when the absorber height was reduced from 7.5 to 1 cm as shown in Figure 6.11c. Nevertheless, as it was mentioned previously, the highest losses were found from the exposed surface because of radiation and convection. Thus, as the maximum temperature was found for the 1 cm collector, the heat flux to the surroundings was higher for the lowest collector height considered. The relatively low heat absorbed and the higher losses led to a lower efficiency as it is shown in Figure 6.11d. The efficiency enhancement was less pronounced for the nanofluid columns larger than 3.8 cm because of the poor transmitted light intensity at the lower section of the receiver. This means that having a higher solar collector for the given specifications will not result in a more efficient receiver.

6.2.6   Influence of the solar concentration

Several researches have proved that reducing the solar concentration minimizes the system cost and offers the possibility of development of a commercially viable product [16]. According to O'Gallagher [32] the maximum solar concentration achievable by using non-imaging optics or sun-tracking is approximately 10 sun. The solar constant, which is an average value measured from satellites, is around 1366 W m^{-2}. Therefore, the solar concentration considered in this study was between 1 to 10 sun.
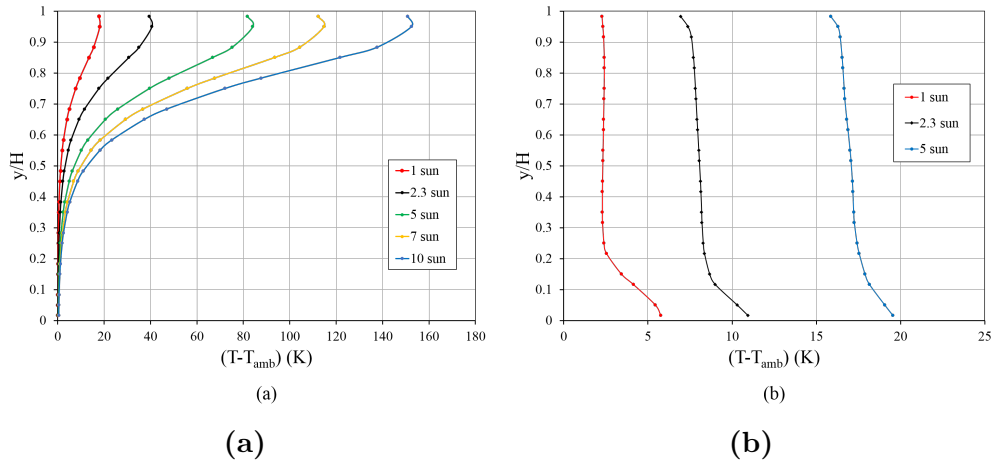
In Figure 6.12a the temperature profiles for different solar concentration when radiating from the top are shown. The maximum temperature, at the top section of the receiver, increases with the solar concentration. However, the temperature at the bottom of the receiver remained constant after 1000 s of exposure even for 10 sun.

The heat absorbed by the nanofluid attenuates as it penetrates along the receiver. The attenuation decreases exponentially and makes the temperature at the bottom to remain stable for all the cases studied after 1000 seconds of exposure. When light incides at the bottom surface, as shown in Figure 6.12b, the maximum temperature is found at the bottom as expected. The temperature gradient at the bottom section is more significant for a lower solar concentration.

The change in temperature with time is illustrated in Figure 6.13 for a 7.5 cm solar collector when radiating from the bottom. Then enhancement
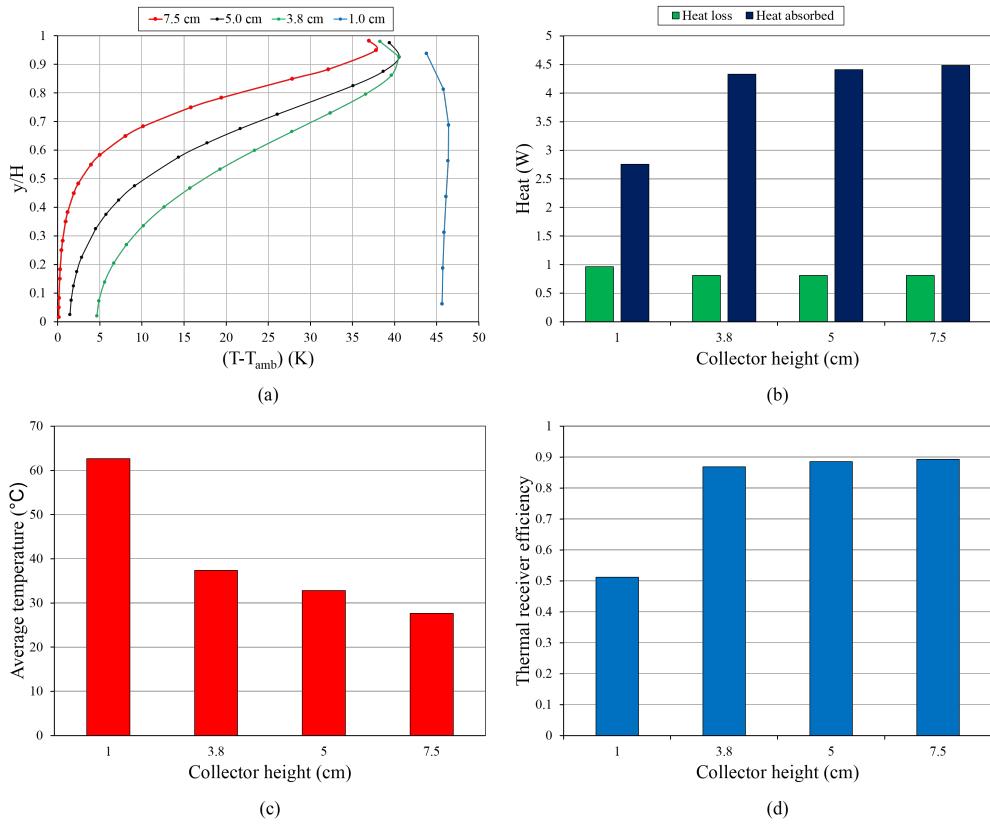
Figure 6.11: Temperature profiles (a); heat loss and absorbed (b); average temperature (c) and efficiency (d) after 1000 s of light exposure for different values of receiver height.


Figure 6.12: Temperature profiles for varying values of solar concentration for: incident light to the top after 1000 s of exposure (a), and incident light to the bottom surface after 600 s of exposure (b).
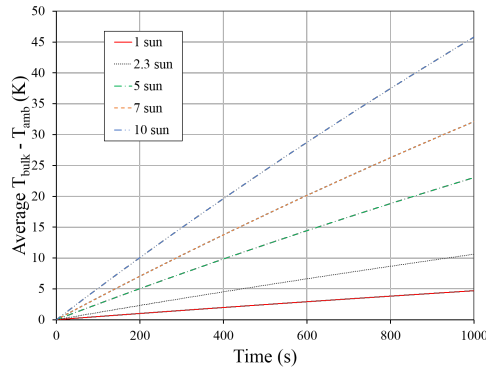
Figure 6.13: Temperature change with time for different values of solar concentration with incident light to the top surface.

in temperature is more pronounced as the solar flux increases.

Figure 6.14 shows the effect of solar concentration on the average temperature enhancement of the receiver. The average temperature of the bulk fluid increases linearly with the irradiance independently of the height of the nanofluid columns studied. This corresponds to the experimental results reported by Chen et al. [24] and previously by Jiang et al. [23] for gold nanoparticles.
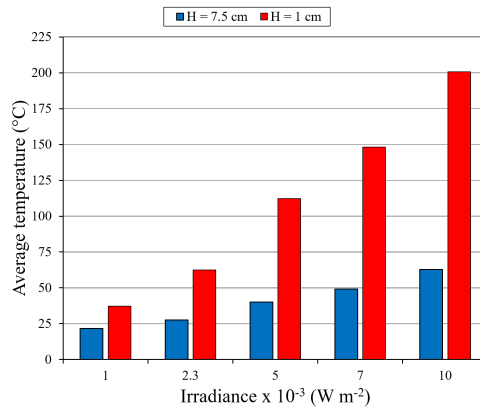
Figure 6.14: Average temperature after 1000 s of incident light to the top surface for various irradiance values.

For 7.5 cm height collector, the efficiency was slightly lower for higher irradiance after 1000 s of exposure (see Figure 6.15.b), while the efficiency when reaching a certain temperature increased with the solar irradiance (Figure 6.15c). The decrease in efficiency with solar intensity for a given time was reported previously by Chen et al. [24]. This inversely behaviour between temperature and efficiency was attributed to limited absorption capability of the nanofluid under high solar intensities. The increment of

38

efficiency with the solar concentration for a given temperature was reported by Liu et al. [17]. For a higher incident heat flux, the temperature of the bulk fluid increased linearly and with that the losses through both, open and insulated surfaces. For a nanofluid height of 1 cm, the average temperature of the bulk fluid increased from 21.70ºC to 200.83ºC when increasing the solar concentration from 1 to 10 sun. For a nanofluid column of 7.5 cm, the temperature enhancement was lower, reaching 62.79ºC for 10 sun. Under a higher solar concentration the temperature enhancement was larger after 1000 s of exposure, as a result the thermal losses from the receiver were also larger. Thus, the thermal efficiency of the receiver did not show a significant increment when rising the solar concentration.
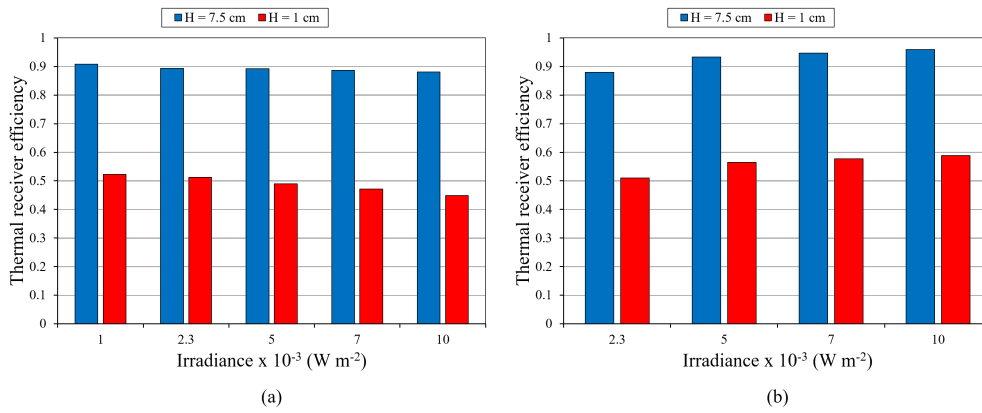
Figure 6.15: Thermal receiver efficiency after 1000 s of exposure to incident light to the top surface (a). Thermal receiver efficiency for at a given temperature as a function of the irradiance (b). $H = 7.5$ cm with $T = 27.6$ºC and $H = 1$ cm with $T = 62.5$ºC.

6.2.7 Influence of the volume fraction

Volume fraction influence on the heat absorption per unit volume in axial direction is presented in Figure 6.16a. As volume fraction increases, the transmitted light intensity into the nanofluid is greater, but it also attenuates faster. Consequently, the absorption capability is limited. For a high volume fraction all the light will be absorbed by a top thin layer [33]. For a volume fraction of 100 ppm the volumetric heat absorbed at the top section was even lower than for 50 ppm. This behaviour is in agreement with the combined experimental and theoretical work by Hogan et al. [34]. For a further increase in volume fraction, they reported a back-scattering off the solution. Figure 6.16b shows the temperature profiles in the axial direction for volume fraction values varying from 0.625 to 10 ppm. The maximum temperature on top of the receiver was found for a volume concentration of 10 ppm, which is congruent with the maximum volumetric heat absorbed.
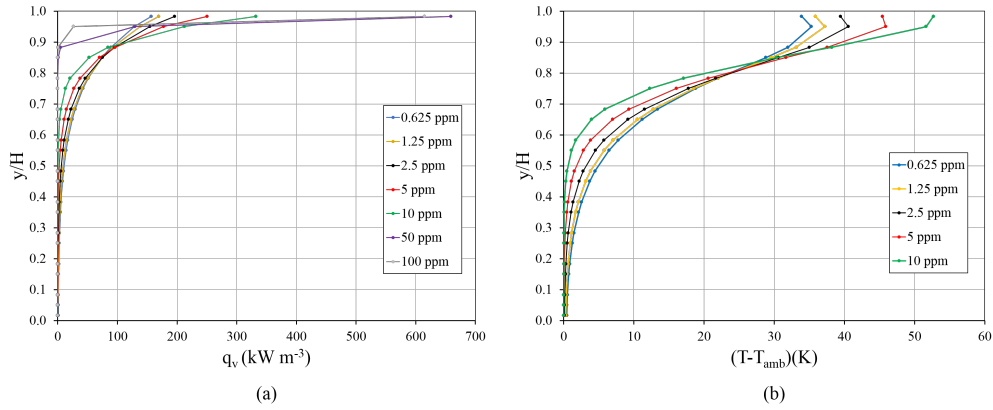
Figure 6.16: Temperature profiles after 1000 s of the heating process for different volume fraction of the dispersed phase.

Figure 6.17 shows the average temperature of the bulk fluid and the thermal receiver efficiency at 1000 s of the heating process for 1 and 7.5 cm height collectors. The average temperature decreases slightly for a higher concentration of the solid particles for a 7.5 cm height solar collector. A maximum average temperature was observed for a volume fraction of around 10-50 ppm for a 1 cm height thermal receiver. This can be explained from the absorption limitation for large amount of particles, as it was introduced previously. The reduction of average temperature with volume fraction was also reported, among others, for $Ag@TiO_2$ nanoparticles [15].

For 7.5 cm height solar collector the efficiency decreased with the volume fraction. As it was mentioned, as the volume fraction increases the light attenuates faster and the temperature gradient increases. The high temperatures were located at the top nanofluid layer where the thermal energy is easily transferred to the surroundings. Accordingly, the losses from the top surface increased with the volume fraction, while the temperature at the bottom remained constant. Thus, a reduction of the average temperature of the bulk fluid with the volume fraction was found for all the range studied and, as a consequence, efficiency decreased with volume fraction. The results present a reduction of approximately 8% on the efficiency when increasing the volume fraction of graphene nanoparticles from 0.625 ppm to 10 ppm. For 1 cm height solar collector the efficiency increased with volume fraction up to 0.005%. The maximum thermal receiver efficiency was about 67%.

Average temperature and thermal receiver efficiency bar graphs comparing the volume fraction effect when incident light is at the bottom or at the top of the receiver are shown in Figure 6.18. A similar trend was ob-

40
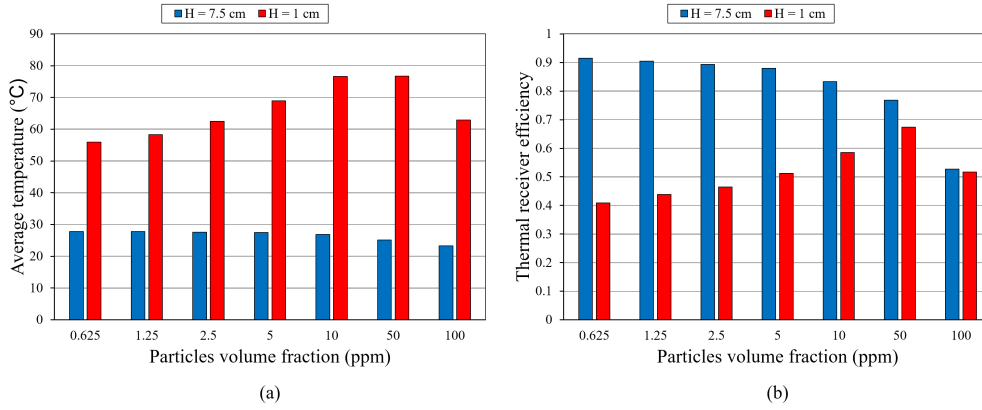
Figure 6.17: Average temperature and efficiency after 1000 s of the heating process with incident light to the top or bottom surface as a function of volume fraction of particles in ppm.
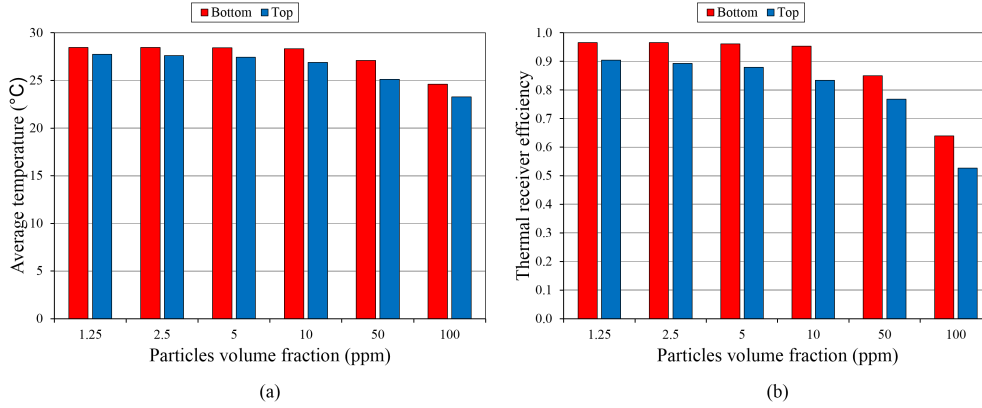
Figure 6.18: Average temperature and efficiency after 1000 s as a function of volume fraction of particles in ppm. H=7.5cm, 2.3 sun, incident light at the bottom surface.

served for both cases, although the reduction of average temperature with the increment in volume fraction was more pronounced with the incident light at the top surface. For this case, the efficiency was reduced by 37% when increasing the volume fraction from 1.25 to 100 ppm. For the bottom surface as the exposed boundary, the reduction was 33%.

Figure 6.19 shows the temperature distribution and the velocity vectors when light is at the bottom of the receiver for 1.25 and 1000 ppm after 1000 s of the heating process. A maximum velocity of 0.15 cm s^{-1} was found for 1.25 ppm, while for 100 ppm the maximum velocity observed was 0.048 cm s^{-1}. This behaviour was also observed by Mirabendin [35] in a CFD modelling study of natural convection heat trasfer of TiO$_2$-water nanofluid. He concluded that as the volume fraction increases, the characteristic convection velocity and the temperature decreases.

41
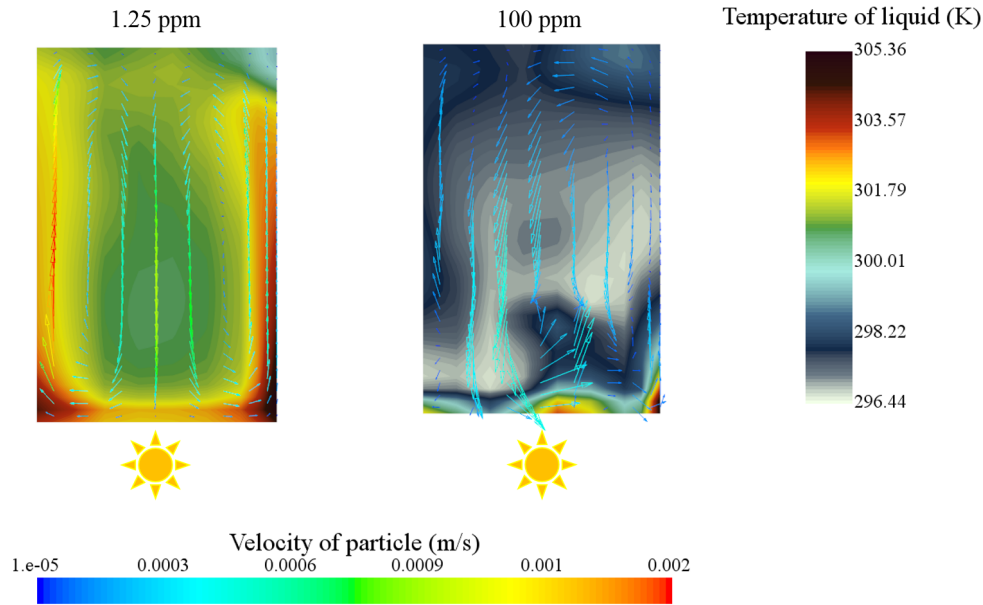
Figure 6.19: Temperature distribution and velocity vectors with incident light to the bottom surface of the receiver for 1.25 and 100 ppm after 1000 s of exposure.

Due to the relatively large time needed to numerically solve the model until equilibrium is reached, several simulations were performed using the steady time solver for varying particle concentration. The steady time solver does not march in time, instead, the solver sets the time dependent terms to zero before it starts running. Thus, the variations of the parameters and the governing equations with time are not considered.

Figure 6.20a shows the effect of volume fraction of the solid particles on the average temperature when the equilibrium has been reached. The equilibrium average temperature of the bulk fluid increases with a decrease in particle concentration. For a volume fraction of 20 ppm, the average temperature was 63.85 K lower than for a volume fraction of 2.5 ppm. This phenomenon is in agreement with the transient time simulation results presented above. The temperature profiles for the same cases are shown in Figure 6.20.b. At equilibrium, the heat absorbed by the nanofluid must equal the losses to the surroundings. The total heat absorbed by the nanofluid decreased insignificantly when increasing the volume fraction from 2.5 to 20 ppm. Thus, the temperature at the top surface was similar for all the cases considered. However, as shown in Figure 6.16 heat absorption was limited to a thin area at the top of the receiver. This was reflected in the temperature profiles. As the volume fraction was reduced, the temperature gradient increased. The heat losses from the side wall were lower

than at the top surface. In consequence, the temperature profile was nearly constant at the bottom section.
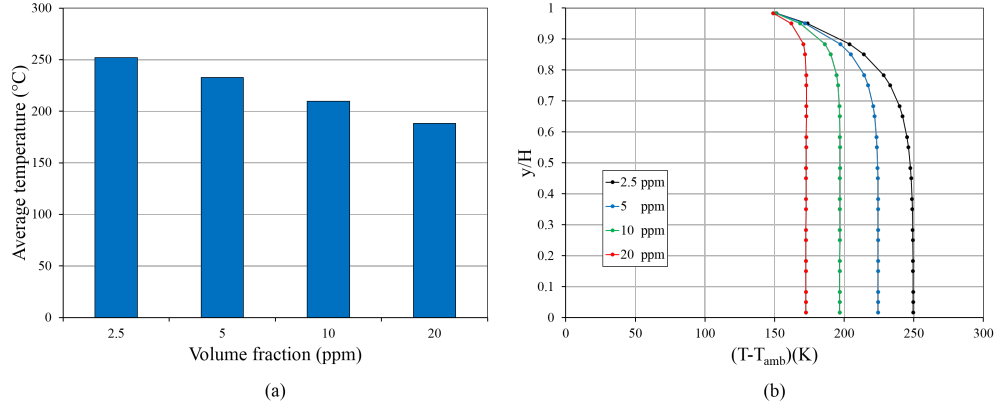
Figure 6.20: Average temperature (a) and temperature profiles (b) comparing various values of particles volume fraction in the range from 2.5 to 20 ppm at the equilibrium state for the stady time solver.

6.2.8 Influence of the particle size
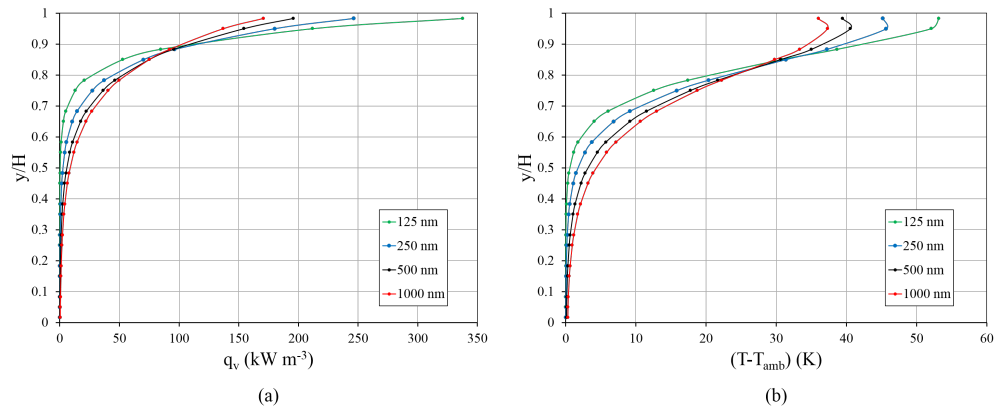
Figure 6.21: Heat absorbed by the nanofluid (a) and temperature profiles (b) in the axial direction after 1000 s of the heating process.

The particle size was varied from 125 to 1000 nm. Figure 6.21a indicates the variation in the heat absorbed by the nanofluid as a function of the diameter of the particles in the axial direction. Contrary to the effect of the volume fraction, by decreasing the size of the nanoparticles, the volumetric heat absorbed gradient increases. The temperature profiles in axial direction, which are illustrated in Figure 6.21b showed a similar trend. A maximum temperature enhancement of 53.2 K was found at the top

43

surface for a volume fraction of 125 ppm, which was reduced to 36 K for a volume fraction of 1000 ppm. This corresponds to previous research work of collectors of millimeter [36] or micrometer order [37]. The temperature at the bottom remained constant during the heating process for the all the concentration values considered in the study.

Average temperature of the bulk fluid and thermal receiver efficiency for different particle diameters are illustrated in Figure 6.22. As the particle diameter increased, the average temperature did not increase considerably, being that increment smaller as the diameter increases. Higher particle sizes absorbed less of the incident energy. The bigger particles were also heavier and deposited at the bottom of the collector, as shown in Figure 6.23. The deeper the particles are found within the nanofluid column, the less light illumination they will absorb.
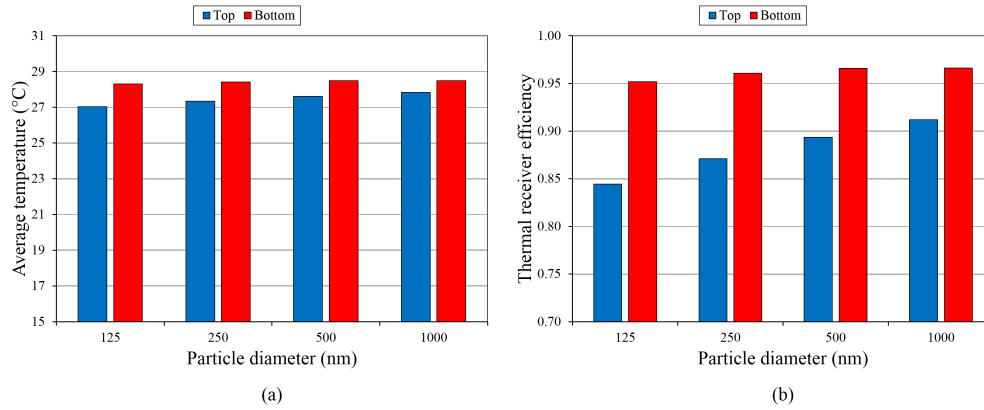
Figure 6.22: Thermal receiver efficiency (a) and average temperature (b) after 1000 s of the heating process as a function of the particles diameter.

The maximum difference in temperature of the phases was found on top of the receiver being 0.0026°C. The maximum relative velocity between the phases was $1.1e^{-6}$ m s^{-1}. This behaviour corresponds to the results from Kalteh et al. [20]. They also reported an uniform distribution of the nanoparticle concentration and concluded that considering the nanofluid as a homogeneous solution was reasonable. However, in the present study, a different volume concentration distribution was found specially when radiating from the top and for larger particle sizes. Figure 6.23 depicts the volume fraction distribution for a particle size of 125 and 1000 nm with incident light to the top and the bottom surfaces. Therefore, it might not be adequate to consider the dispersed phase in the nanofluid as homogeneous distributed for this application.

The Brownian source was reduced as the size of the particles increased, as it was revealed by Habib and Roghayyeh [38] in their numerical study
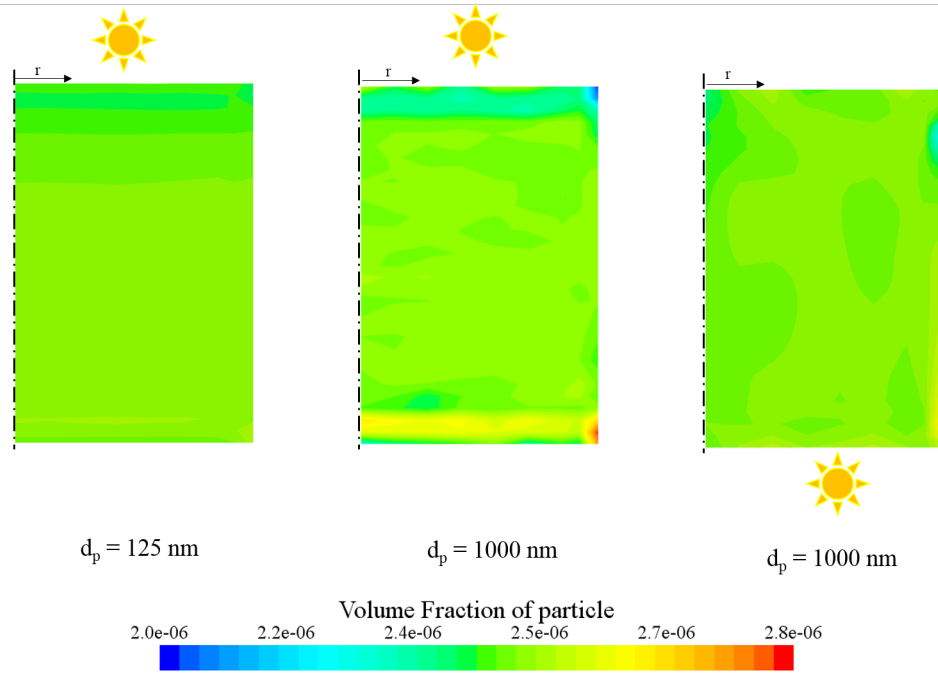
Figure 6.23: Volume fraction distribution for particle size of 1 μm (right) and 125 nm (left) after 1000 s of exposure to incident light to the top and to the bottom surface.

using the Eulerian-Lagrangian approach. For 1000 nm particles the maximum Bownian force was around 0.3 N while for 250 nm was 4.8 N. As it is applied to the opposite direction of the concentration gradient, it influences the distribution of the particles.

Chapter 7

Conclusions and further work

An Eulerian two-phase model was developed for simulating photothermal conversion in nanofluids in a DAC. The Brownian motion was included in the model as interphase momentum exchange. The volumetric absorption of the Sun light was modeled according to the Beer-Lambert law.

The accuracy of the model was satisfactory. The most important discrepancies appeared due to the fact that the nanofluid extinction coefficient was assumed independent of the radiation wavelength.

The enhancement in efficiency due to the use of nanofluids was demonstrated by comparison against a selective surface absorption collector. The efficiency of the DAC using a nanofluid as the absorber was 20% greater than for a surface absorber.

The extinction coefficient, the volume fraction and the diameter of the particles are parameters, which influence the heat absorbed by the nanofluid. Reducing the extinction coefficient of the base fluid from 80 to 20 m^{-1} led to an increase of 2.7% in the thermal receiver efficiency. The radiative and convective losses from the DAC surfaces were increased with the nanoparticle volume fraction. For 1 cm absorber and incident light to the top of the receiver, the maximum efficiency (67%) was found at 50 ppm. The enhancement in efficiency when increasing the diameter of the particles from 125 to 1000 nm was lower than 7%. Deposition of the 1000 nm particles was observed after 1000 s of the heating process with incident light to the top surface.

As the specific heat decreased, the losses to the surroundings and the efficiency increased. An efficiency reduction of 43% was observed when the collector height was reduced from 7.5 to 1.0 cm. A maximum average temperature of the bulk fluid of 200.8°C was found for a nanofluid column of 1 cm and 10 sun. For a nanofluid height of 7.5 cm the maximum temperature after 1000 s of exposure was 62.8°C.

A strong dependency on the size of the nanofluid column and convection

currents was shown. Comparing the cases with incident light to the bottom and to the top surface, the efficiency was enhanced by 14.5%. With incident light to the bottom surface, the maximum velocity of the particles was observed for 1.25 ppm.

In conclusion, a reliable theoretical model describing the effect of different parameters has been presented. Based on the parametrical analysis accomplished for graphene nanoparticles dispersed in [HMIM]BF$_4$, the concentration of the Sun light should be as large as possible when designing a DAC. For the rest of the parameters, two different guidelines are recommended whether the purpose is heating or steam generation:

- For heating applications, it is recommended to focus the light towards the bottom surface in order to reach a higher average temperature and lower losses to the surroundings. The maximum height should not exceed 3.8 cm because of the attenuation of the light. A low volume fraction improves the stirring of the nanofluid and for a nanofluid column of 1 cm should not be larger than 10 ppm. As the efficiency and temperature enhancement was not relatively significant when increasing the particle size, it is advisable to use particles smaller than 500 nm to avoid deposition and other problems in the equipment.

- For steam generation, a design with incident light to the top surface is proposed so that larger temperatures are confined to the exposed surface. A lower nanofluid column will assure higher temperatures. The volume fraction is to be restricted to 50 ppm because of the light absorption limitation.

Regarding the choice of the base fluid, for heating application a high specific heat should be considered. For steam generation applications, a base fluid with extinction coefficient of about 70 m^{-1} and low specific heat and its variation with temperature is suggested.

Further investigation might focus on the performance of the model when including other effects such as the presented below:

- Model of the extinction coefficient as a function of the radiation wavelength.

- Non-spherical particles.

- Particle size distribution model instead of using a constant size.

- The agglomeration of the particles.

- Account for the viscosity of the nanofluid, which depends on the size and concentration of the nanoparticles.

- Effect of magnetic field to attract the particles towards the most convenient surface.

Bibliography

[1] European Commission. Communication from the commission to the European parliament, the council, the European economic and social committee and the committee of the regions. A policy framework for climate and energy in the period from 2020 to 2030. *European Commission, Brussels*, 2014.

[2] E. Kabir, P. Kumar, S. Kumar, A.A. Adelodun and K. Kim. Solar energy: Potential and future prospects. *Renewable and Sustainable Energy Reviews*, 82:894–900, 2018.

[3] Eurostat. Renewable energy sources. Figure 4: Gross inland consumption of renewables EU-28 1990-2016. Retrieved from http://ec.europa.eu/eurostat/statistics−explained/index.php?title= File:Figure_4−Gross_inland_consumption_of_renewables_EU−28_1990 −2016.png.

[4] P. Raj and S. Subudhi. A review of studies using nanofluids in flat-plate and direct absorption solar collectors. *Renewable and Sustainable Energy Reviews*, 84:54–74, 2018.

[5] S.U.S. Choi, J.A. Eastman. Enhancing thermal conductivity of fluids with nanoparticles. *Proceedings of the ASME International Mechanical Engineering Congress and Exposition*, 66:99–105, 1995.

[6] S. Iranmanes, H.C. Ong, B.C. Ang, E. Sadeghinez, A. Esmaeilzadeh, M. Mehrali. Thermal performance enhancement of an evacuated tube solar collector using graphene nanoplatelets nanofluid. *Cleaner Production*, 162:121–129, 2017.

[7] M. Lomascolo, G. Colangelo, M. Milanese, A. De Risi. Review of heat transfer in nanofluids: Conductive, convective and radiative experimental results. *Renewable and Sustainable Energy Reviews*, 43:1182–1198, 2015.

[8] D. Han, Z. Meng, D. Wu, C. Zhang and H. Zhu. Thermal properties of carbon black aqueous nanofluids for solar absorption. *Nanoscale Research Letters*, 6:457, 2011.

[9] O. Neumann, A.S. Urban, J. Day, S. Lal, P. Nordlander and N.J. Halas. Solar vapor generation enabled by nanoparticles. *ACS Nano*, 7:42–49, 2013.

[10] S.F. Ahmed, M. Khalid, W. Rashmi, A. Chan, K. Shahbaz. Recent progress in solar thermal energy storage using nanomaterials. *Renewable and Sustainable Energy Reviews*, 67:450–460, 2017.

[11] M. Faizal, A. Bouazza and R.M. Singh. Heat transfer enhancement of geothermal energy piles. *Renewable and Sustainable Energy Reviews*, 57:16–13, 2016.

[12] C.T. Crowe, J.D. Schwarzkopf, M. Sommerfeld and Y. Tsuji. *Multiphase Flows with Droplets and Particles*. CRC Press, 2011.

[13] J.D. Anderson. *Computational fluid dynamics : the basics with applications*. McGraw-Hill, 1995.

[14] H. Ryagi and P. Phelan. Predicted efficiency of a low-temperature nanofluid-based direct absorption solar collector. *Journal of Dispersion Science and Technology*, 32:1311–1317, 2011.

[15] H. Li, Y. He, Z. Liu, Y. Huang and B. Jiang. Synchronous steam generation and heat collection in a broadband Ag@TiO^2 core–shell nanoparticle-based receiver. *Applied Thermal Engineering*, 121:617–627, 2017.

[16] G. Ni, N. Miljkovic, H. Ghasemi, X. Huang, S.V.Boriskina, C. Lin, J.J. Wang, Y. Xu, Md.M. Rahman, T, Zhang and G. Chen. Volumetric solar heating of nanofluids for direct vapor generation. *Nano Energy*, 17:290–301, 2015.

[17] J. Liu, Z. Ye, L. Zhang, X. Fang and Z. Zhang. A combined numerical and experimental study of graphene/ionic liquid nanofluid based direct absorption solar collector. *Solar Energy Materials & Solar Cells*, 136:177–186, 2005.

[18] Sh.M. Vanaki, P. Ganesan and H.A. Mohammed. Numerical study of convective heat transfer of nanofluids: A review. *Renewable and Sustainable Energy Reviews*, 54:1212–1239, 2016.

[19] M. Mahdavi, M. Sharifpur and J.P. Meyer. CFD modelling of heat transfer and pressure drops for nanofluids through vertical tubes in laminar flow by lagrangian and eulerian approaches. *International Journal of Heat and Mass Transfer*, 88:803–813, 2015.

[20] M. Kalteh, A. Abbassi, M. Saffar-Avval and J. Harting. Eulerian-Eulerian two-phase numerical simulation of nanofluid laminar forced convection in a microchannel. *International journal of heat and fluid flow*, 32:107–116, 2010.

[21] M. Kalteh, A. Abbassi, M. Saffar-Avval, A. Frijns, A. Darhuber and J. Harting. Experimental and numerical investigation of nanofluid forced convection inside a wide microchannel heat sink. *Applied Thermal Engineering*, 36:260–268, 2012.

[22] F. Wang, L. Han, Z. Zhang, X. Fang, J. Shi and W. Ma. Surfactant-free ionic liquid-based nanofluids with remarkable thermal conductivity enhancement at very low loading of graphene. *Nanoscale Research Letters*, 7:314, 2012.

[23] K. Jiang, D.A. Smith and A. Pinchuk. Size-dependent photothermal conversion efficiencies of plasmonically heated gold nanoparticles. *Journal of Physical Chemistry*, 117:27073–27080, 2013.

[24] M. Chen, Y. He, J. Huang and J. Zhu. Investigation into Au nanofluids for solar photothermal conversion. *International Journal of Heat and Mass Transfer*, 108:1894–1900, 2017.

[25] Star-CCM+. User guide for version 12.02. *Siemens PLM Software Simcenter*, 2017.

[26] S. Dong, L. Zheng, X. Zhang, S. Wu and B. Shen. A new model for Brownian force and the application to simulating nanofluid flow. *Microfluidics and Nanofluidics*, 16:131–139, 2014.

[27] V. Rastegar, G. Ahmadi and S.V. Babu. Filtration of aqueous colloidal ceria slurries using fibrous filters - An experimental and simulation study. *Separation and Purification Technology*, 176:231–242, 2017.

[28] M. Liberman, N. Kleeorin, I. Rogachevskii and N.E.L. Haugen. Mechanism of uncon ned dust explosions: Turbulent clustering radiation-induced ignition. *Physical Review E*, 95:051101, 2017.

[29] M. Bahiraei and M. Hangi. Flow and heat transfer characteristics of magnetic nanofluids: A review. *Journal of Magnetism and Magnetic Materials*, 374:125–138, 2015.

[30] P.Bermel, J.Lee, J.D.Joannopoulos, I.Celanovic, M.Soljacic. Selective solar absorbers. *Annual Review of Heat Transfer*, 15:231–254, 2012.

[31] V. Khullar, H. Tyagi, N. Hordy, T. P.Otanicar, Y. Hewakuruppu, P. Modi and R.A. Taylor. Harvesting solar thermal energy through nanofluid-based volumetric absorption systems. *International Journal of Heat and Mass Transfer*, 77:377–384, 2014.

[32] J.J. O'Gallagher. *Nonimaging optics in solar energy*. 2008.

[33] R.A. Taylor, P.E. Phelan, T.P. Otanicar, R. Adrian and R. Prasher. Nanofluid optical property characterization: towards efficient direct absorption solar collectors. *Nanoscale Research Letters*, 6:225, 2011.

[34] N.J. Hogan, A.S. Urban, C. Ayala-Orozco, A. Pimpinelli, P. Nordlander and N.J. Halas. Nanoparticles heat through light localization. *Nano letters*, 14:4640–4645, 2014.

[35] S. Mirabedin. CFD modeling of natural convection heat transfer of TiO_2-water nanofluid in a cylindrical container. *Frontiers in Heat and Mass Transfer*, 7:17, 2016.

[36] T.E. Amin, G. Roghayeh, R.Fatemeh and P. Fatollah. Experimental and numerical investigation of nanofluid forced convection inside a wide microchannel heat sink. *Energy Exploration & exploitation*, 33:659–676, 2015.

[37] T.P. Otanicar, P.E. Phelan, R.S. Prasher, G. Rosengarten and R.A. Taylor. Nanofluid-based direct absorption solar collector. *Journal of Renewable and Sustainable Energy*, 2:033102, 2010.

[38] H. Aminfar and R. Motallevzadeh. Numerical investigation of the effects of nanoparticle diameter on velocity field and nanoparticle distribution of nanofluid using Lagrangian-Eulerian approach. *Journal of Dispersion Science and Technology*, 32:1311–1317, 2011.

Appendix A

Publication

Eulerian-Eulerian Model for Photothermal Energy Conversion in Nanofluids

M. Lucas, P. Kosinski, B.V. Balakin

Eulerian-Eulerian Model for Photothermal Energy Conversion in Nanofluids

Melodía Lucas[1,a)], Pawel Kosinski[1] and Boris V. Balakin[2,3]

[1]*University of Bergen, Department of Physics and Technology, Allegt. 55, 5007 Bergen, Norway*
[2]*NRNU Moscow Engineering Physics Institute, Kashirskoe shosse, 31, 115409 Moscow, Russia*
[3]*Western Norway University of Applied Sciences, Inndalsveien 28, 5063 Bergen, Norway*

[a)]Corresponding author: melodialucas@gmail.com

Abstract. In this research photothermal energy conversion in nanofluids was numerically studied using a CFD model. A Direct Absorption Collector (DAC) of cylindrical shape with incident light on one of its surfaces was adopted for the simulations. The Eulerian two-phase transient model included the volumetric absorption of light, losses to the surroundings and the Brownian motion. The simulation results were validated with experimental data, demonstrating modest discrepancies. The model was studied parametrically, altering particle volume fraction, collector height and surface transparency. We found that: the efficiency drops by 43% when the absorber height is reduced from 7.5 to 1.0 cm for 2.5 ppm; the maximum efficiency was 67% at 50 ppm (1 cm absorber); the efficiency of the DAC with nanofluid is 20% greater than the efficiency for the surface absorber; natural convection in the collector improves the efficiency by 7%.

INTRODUCTION

The fact that the Sun is a major source of inexhaustible energy makes solar power technologies one of the key solutions for the increasing demand of energy. However, due to the relatively low efficiency of conventional solar harvesters (collectors, ponds and photovoltaic cells), use of solar energy is challenging. One of the ways to improve their performance is the use of nanofluids. In the last decades several experimental studies have shown the enhancement of the thermal performance by adding nano-size particles to the working fluid. Still a better understanding on thermophysical properties, thermal and flow behaviour of nanofluids is needed for the development of new more efficient technologies.

Jian et al. [1] developed a heat transfer model to predict the temperature and efficiency of a DAC and compared the model with their experimental results. They attributed temperature discrepancies between numerical and experimental results to convection effects not considered in the model. The most common approach among theoretical studies of nanofluids has been the single-phase approach, which assumes thermal equilibrium between the phases and neglects the slip mechanisms between a nano-particle and the host fluid. The results, however, are strongly dependent on the effective parameters models obtained from experimental work. Mahdavi et al. [2] performed a numerical study of the hydrodynamic behaviour of nanofluids. They compared the Eulerian mixture model with the Lagrangian model in a steady-state flow. The first one solves only one momentum and one energy equation, while the last one calculates the slip velocity and temperature difference between particles and liquid. For the mixture model, a strong dependency on the empirical properties of nanofluid was reported. The Lagrangian approach, which only requires thermophysical properties for the base fluid, showed a better agreement with experiments. Nevertheless, a large number of nanoparticles present in the nanofluids, even for a low volume concentration, makes the Lagrangian technique hardly applicable for a numerical simulation of the nanofluid-supported DAC, due to enormous computational costs. Kalteh et al. [3] used an Eulerian-Eulerian two-phase model to study the laminar forced convection heat transfer of a nanofluid inside an isothermally heated microchannel. They included a virtual mass force and a particle-particle interaction force in their model. They observed a negligible relative velocity and temperature between the phases and concluded that the under-estimation of the heat transfer enhancement by single-phase approaches is due to the models for the nanofluid properties assumed.

In the present contribution, a transient Eulerian-Eulerian model was adopted to study the photo-thermal conversion in a DAC under low solar concentration. The volumetric absorption of incident light and the Brownian motion models were included. The effects of particle concentration, height of collector and natural convection on the thermal efficiency were studied.

MODEL

The model presented in the following reproduces the experimental work by Jian et al. [1]: a cylindrical DAC of 10 cm diameter and 7.5 cm height. The Eulerian-Eulerian two-phase model was adopted, which assumes the phases as continuous fluids coexisting in the domain with the volume fraction, φ, specifying the volume occupied by each phase, $i=f$ (base fluid) and $i=p$ (nanoparticles). The continuity and momentum equations read:

$$\frac{\partial(\varphi_i\rho_i)}{\partial t} + \nabla(\varphi_i\rho_i\mathbf{v}) = 0 \qquad \text{and} \qquad \frac{\partial(\varphi_i\rho_i\mathbf{v}_i)}{\partial t} + \nabla(\varphi_i\rho_i\mathbf{v}_i\mathbf{v}_i) = -\varphi_i\nabla p + \nabla(\varphi_i\mu_i\mathbf{v}_i) + \varphi_i\rho_i\mathbf{g} + \mathbf{F}_{D,i} + \mathbf{F}_{B,i}, \qquad (1)$$

where ρ is the density, $\mathbf{v}$ is the velocity vector, p is the static pressure field, μ is the dynamic viscosity, $\mathbf{g}$ is the gravitational field, and $\mathbf{F}_D$ is drag force calculated using the Schiller-Naumann correlation and corrected by the Cunningham factor, C_c [4].

The Brownian motion term in the momentum equation, $\mathbf{F}_B$, reads [5]:

$$\mathbf{F}_{B,i} = nm_p\xi\sqrt{\frac{216\nu k_B T_f}{\pi\rho_f d_p^5(\frac{\rho_p}{\rho_f})^2 C_c\Delta t}}, \qquad (2)$$

where n is the number density, m_p is the mass of one particle, ξ is a vector of zero-mean, unit-variance-independent Gaussian random numbers, ν is the kinematic viscosity of the fluid, k_B is the Boltzmann constant, T_f is the absolute temperature of the base fluid, d_p is the diameter of the particles and Δt is the integration time step.

The energy equation is written as:

$$\frac{\partial(\varphi_i\rho_i e_i)}{\partial t} + \nabla(\varphi_i\rho_i e_i\mathbf{v_i}) = \nabla(\varphi_i k_f\nabla T_i) - \frac{6k_f Nu\varphi_p}{d_p^2}(T_i - T_j) + q_{v,i}. \qquad (3)$$

Here e is the specific energy, k_f is the thermal conductivity of the fluid, Nu is calculated using the Ranz-Marshall correlation and q_v is the volumetric heat generation calculated as: $q_{v,i} = \varphi_i I_0 K_i \exp\left(-\left(K_f + K_p\right)y\right)$, where $I_0 = 2300$ W m^{-2} is the light intensity, y refers to the optical path, K_f is the extinction coefficient of the base fluid and $K_p = 6\varphi_p/d_p$ is the extinction coefficient of the particles [6].

Figure 1a presents the geometry and the boundary conditions. The exposed boundary refers to the surface, which receives the light. A mixed convective and radiative boundary condition was used to model the exposed surface prescribed following Jian et al. [1]. The opposite surface was assumed to be adiabatic and at the side surface a convective boundary was considered. The no-slip boundary condition was assumed for both phases at all the surfaces. In addition, two symmetry planes were applied to reduce the computational domain to a quarter of cylinder. The initial conditions included: uniform temperature field 290.15 K, zero velocity and atmospheric pressure.

The thermal efficiency of the solar receiver is defined as a ratio between the collected thermal energy to the total incident energy [1]: $\eta = \left(mc_p(\bar{T}_f - T_{amb})\right)/\left(\int_0^t I_0 A dt\right)$.

The numerical model was built in the commercial software Star-CCM+. The discretization of the governing equations in space was done by a finite volume technique with 3840 hexahedral cells and an implicit advancement in time with a step of 5 ms. The equations were solved using the SIMPLE numerical technique.

RESULTS AND DISCUSSIONS

Figure 1b shows the comparison of simulations with experiments [1]. The temperature at the bottom of the collector when the top is exposed to the Sun radiation remained constant even after 1000 s of exposure, leading to a more pronounced temperature gradient with time. This behaviour was expectable since the light beam attenuates as it travels
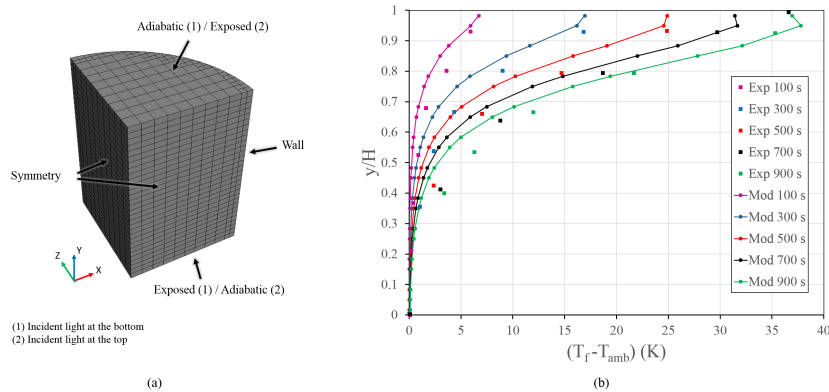
FIGURE 1. Mesh and boundary conditions (a). Nanofluid temperature profile in axial direction. Simulation results (Mod) are compared with experiments (Exp) at 100, 300, 500, 700 and 900 s of the heating process (b). H=7.5 cm, φ_p=2.5 ppm, d_p= 500 nm.
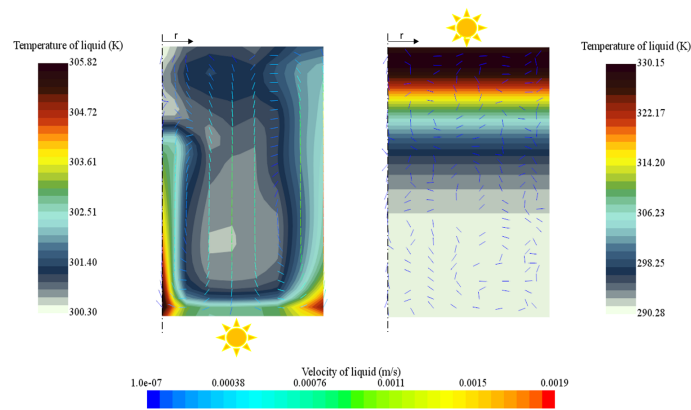

FIGURE 2. Temperature distribution and velocity vectors when incident light is at the bottom (left) and at the top of the receiver (right) after 1000 s of exposure.

through the nanofluid column according to the Beer-Lambert law. The discrepancies with the model were lower than 8% and can be attributed to the assumption of the constant extinction coefficient over the full wavelength spectrum.

Figure 2 shows the temperature distribution and vectors of the nanoparticle velocity in the midline cross-section of the DAC. For the case with incident light at the top surface, the velocity is negligible and the temperature variation along the y-axis is significant. With incident light at the bottom surface, convective currents were found during the simulation, which lead to a more uniform temperature profile. The temperature difference between the top and bottom surfaces was reduced from 39.3 to 3.4 K, so that the losses to the surroundings were limited.

To elucidate the benefits of the volumetric absorption in DACs when using nanofluids, the results are compared to a surface absorption collector in Figure 3a. In the latter case, the volumetric heat generation was set to zero and a heat flux of $I_0\alpha$ W m^{-2} was delivered at the exposed boundary. As a result, the thermal receiver efficiency is enhanced over 20% for the volumetric absorption receiver for both cases considered: incident light on top or bottom surface. Even though the emissivity of solar selective surfaces is much lower than for nanofluids [7], the localization of high temperatures to the interior of the receiver resulted in lower radiative losses in the case of the volumetric absorption.

For a larger collector height, the nanofluid absorbs more of the incident light as shown in Figure 3b, while the temperature at the surfaces was found to be lower. Due to the insulation at the sides of the receiver, the higher losses are found from the non-insulated surface because of radiation and convection. Therefore, the thermal efficiency of the receiver was enhanced for the larger collector height. For 1 cm height solar collector the efficiency increased with volume fraction up to 0.005%. As volume fraction increases, the transmitted light intensity into the nanofluid is greater,
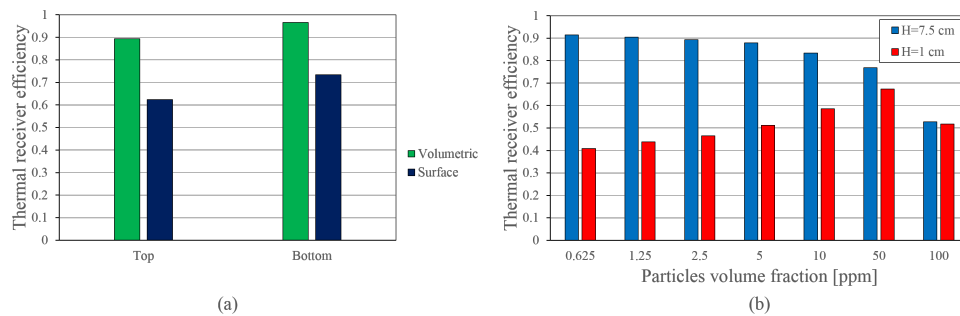
FIGURE 3. Thermal receiver efficiency comparison at 1000 s for: (a) volumetric and surface absorption, considering a selective surface with absorption 0.8 and emissivity 0.12 [9]; (b) 7.5 and 1 cm height solar receiver for different particle volume fraction.

but it also attenuates faster. Consequently, the absorption capability is limited. For a high volume fraction all the light will be absorbed by a top thin layer where the thermal energy is easily transferred to the surroundings [8]. Accordingly, for a 7.5 cm nanofluid column, the temperature gradient and losses from the top surface will increase with the volume fraction, while temperature at the bottom remains constant. Thus, a reduction of the average temperature of the bulk fluid with the volume fraction was found for all the range studied and, as a consequence, efficiency decreases with volume fraction.

CONCLUSIONS

An Eulerian two-phase model was developed to study nanofluids in a DAC. The enhancement in efficiency due to the use of nanofluids was demonstrated by comparison against a selective surface absorption collector, 20% enhancement was found. A strong dependency on the size of the nanofluid column and convection currents was shown. The efficiency decreased by 43% when the collector height was reduced from 7.5 to 1.0 cm. The radiative and convective losses from the DAC surfaces were increased with the nanoparticle volume fraction. For 1 cm absorber, the maximum efficiency (67%) was found at 50 ppm. The accuracy of the model was satisfactory. The most important discrepancies appeared due to the fact that the nanofluid extinction coefficient was assumed independent of the radiation wavelength. Further research should focus on the performance of the model when taking into account other effects such as agglomeration, particle size distribution or use of non-spherical particles.

ACKNOWLEDGEMENTS

REFERENCES

[1] L. Zhang X. Fang J. Liu, Z. Ye and Z. Zhang. *Solar Energy Materials & Solar Cells*, 136:177–186, 2005.
[2] J.P. Meyer M. Mahdavi, M. Sharifpur. *International Journal of Heat and Mass Transfer*, 88:803–813, 2015.
[3] M. Saffar-Avval adn J. Harting M. Kalteh, A. Abbassi. *International Journal of Heat and Fluid Flow*, 32:107–116, 2011.
[4] M. Sommerfeld C.T. Crowe, J.D. Schwarzkopf and Y. Tsuji. *Multiphase Flows with Droplets and Particles*. CRC Press, 2011.
[5] X. Zhang-S. Wu S. Dong, L. Zheng and B. Shen. *Microfluidics and Nanofluidics*, 16:131–139, 2014.
[6] I. Rogachevskii-N.E.L Haugen M. Liberman, N. Kleeorin. *Phys. Rev. E*, 95:051101, 2017.
[7] N. Hordy-T. P.Otanicar Y. Hewakuruppu P. Modi R. A.Taylor V. Khullar, H. Tyagi. *International Journal of Heat and Mass Transfer*, 77:377–384, 2014.
[8] T. P. Otanicar R. Adrian R. A. Taylor, P. E. Phelan and R. Prasher. *Nanoscale Research Letters*, 6:225, 2011.
[9] J. D. Joannopoulos I. Celanovic M. Soljacic P. Bermel, J. Lee. *Annual Review of Heat Transfer*, 15:231–254, 2012.